

Mapping circuit dynamics during function and dysfunction

Srinivas Gorur-Shandilya¹, Elizabeth M. Cronin², Anna C. Schneider², Sara Ann Haddad^{1†}, Philipp Rosenbaum^{1‡}, Dirk Bucher², Farzan Nadim², Eve Marder¹

*For correspondence:
marder@brandeis.edu (EM)

Present address: [†]Department of Molecular Life Sciences, University of Zürich, Switzerland; [‡]GlobalData, USA

¹Volen Center and Biology Department, Brandeis University, Waltham MA 02454 USA;
²Federated Department of Biological Sciences, New Jersey Institute of Technology and Rutgers University, 323 Martin Luther King Blvd, Newark, NJ 07102

Abstract

Neural circuits can generate many spike patterns, but only some are functional. The study of how circuits generate and maintain functional dynamics is hindered by a poverty of description of circuit dynamics across functional and dysfunctional states. For example, although the regular oscillation of a central pattern generator is well characterized by its frequency and the phase relationships between its neurons, these metrics are ineffective descriptors of the irregular and aperiodic dynamics that circuits can generate under perturbation or in disease states. By recording the circuit dynamics of the well-studied pyloric circuit in *C. borealis*, we used statistical features of spike times from neurons in the circuit to visualize the spike patterns generated by this circuit under a variety of conditions. This unsupervised approach captures both the variability of functional rhythms and the diversity of atypical dynamics in a single map. Clusters in the map identify qualitatively different spike patterns hinting at different dynamical states in the circuit. State probability and the statistics of the transitions between states varied with environmental perturbations, removal of descending neuromodulation, and the addition of exogenous neuromodulators. This analysis reveals strong mechanistically interpretable links between complex changes in the collective behavior of a neural circuit and specific experimental manipulations, and can constrain hypotheses of how circuits generate functional dynamics despite variability in circuit architecture and environmental perturbations.

Introduction

Neural circuits can generate a wide variety of spiking dynamics, but must constrain their dynamics to function appropriately. Cortical circuits maintain irregular spiking patterns through a balance of excitatory and inhibitory inputs (*van Vreeswijk and Sompolinsky, 1996; Mariño et al., 2005; Brunel and Wang, 2003*) and the loss of canonical dynamics is associated with neural diseases like channelopathies and epilepsy (*Marbán, 2002; Staley, 2015*). Preserving functional dynamics can be a challenge for neural circuits for the following reasons. The same spike pattern can be generated by diverse circuits with many different topologies and broadly distributed synaptic and cellular parameters (*Prinz et al., 2004; Golowasch et al., 2002; Alonso and Marder, 2019*). Furthermore, neural circuits are constantly being reconfigured, with ion channel protein turnover, and homeostatic feedback mechanisms modifying conductance and synapse strengths continuously (*Turrigiano et al., 1994, 1995; O'Leary et al., 2014; Franci et al., 2020*). The problem of maintaining functional activity patterns is aggravated by the fact that functional circuit dynamics tend to lie within a low-dimensional subspace within the high-dimensional state space: of the numerous possible solutions, only a few are functional and are found in animals (*Cunningham and Yu, 2014*;

43 **Pang et al., 2016**). How do neural circuits preserve functional dynamics despite these obstacles?
44 Answering this question requires, as a prerequisite, a quantitative description of the dynamics of
45 neural circuits during function and dysfunction. When rhythms are regular, this is relatively simple,
46 but when rhythms become irregular, classifying them becomes hard (**Haddad and Marder, 2018**;
47 **Tang et al., 2012**; **Haley et al., 2018**). In this paper we study the dynamics of a well-studied central
48 pattern generator, the pyloric circuit in the stomatogastric ganglion in *C. borealis* (**Marder and**
49 **Bucher, 2007**). The pyloric circuit is small, in crabs consisting of 13 neurons coupled by inhibitory
50 and electrical synapses. Its topology and cellular dynamics are well understood, and the circuit
51 generates a clearly defined "functional" collective behavior where bursts of spikes from three
52 different cell types alternate rhythmically to generate a triphasic motor pattern. The stereotypy and
53 periodicity of the motor pattern suggests that the dynamics of the pyloric circuit are fundamentally
54 low dimensional. This has allowed for the effective parameterization of the rhythm by a small
55 number of *ad-hoc* descriptors such as the burst period, duty cycles, and phase of each neuron
56 (**Hartline and Maynard, 1975**; **Eisen and Marder, 1984**; **Miller and Selverston, 1982**).

57 In response to prolonged perturbations, pyloric circuit dynamics are not always periodic, and
58 descriptors that work well to characterize the canonical rhythm are inadequate to describe these
59 atypical dynamical states. Efforts to study circuit dynamics under these regimes, and to characterize
60 how the circuit responds to, and recovers from perturbations, have been frustrated by the inability
61 to quantitatively describe irregular and non-stationary dynamics (**Haddad and Marder, 2018**; **Tang**
62 **et al., 2012**; **Haley et al., 2018**).

63 In this paper we set out to address the problem of quantitatively describing neural circuit dynam-
64 ics under a variety of conditions. We reasoned that circuit dynamics lie on some lower dimensional
65 set within the full high dimensional space of possible dynamics, even when circuits exhibit atypical
66 and non-functional behavior, because even circuits generating dysfunctional dynamics are still
67 constrained by cellular parameters and network topology. We therefore set out to find and visualize
68 this subset of spike patterns using an unsupervised machine learning approach. This unsuper-
69 vised method allows us to visualize the totality of a large and complex data set of spike patterns,
70 while being explicit about the assumptions and biases in the analysis. Using this method, we
71 found non-trivial spiking patterns in the distribution of the data that hinted at diverse, stereotyped
72 responses to perturbations. By classifying these patterns, and measuring transitions between
73 these patterns, we were able to characterize the diversity of circuit dynamics under baseline and
74 perturbed conditions, and to identify anecdotally observed atypical states within the full repertoire
75 of spiking patterns (for many hundreds of animals).

76 Results

77 Perturbations can destabilize the triphasic pyloric rhythm

78 Studies that measure the pyloric rhythm commonly involve recording from nerves from the stomato-
79 gastric ganglion (STG) in ex-vivo preparations. Preparations typically also include the stomatogastric
80 nerve (*stn*) that carries the axons of descending neuromodulatory neurons from the oesophageal
81 and commissural ganglia that project into the STG. Under baseline conditions (11°C, with the *stn*
82 intact, **Figure 1a**), the periodic triphasic oscillation of the pyloric circuit can be measured by extra-
83 cellular recordings of the *lpn*, *pdn* and *pyn* nerves (**Figure 1a**). Bursts of PD spikes on the *pdn* are
84 followed by bursts of LP spikes on *lpn* and bursts of PY spikes on *pyn*. Spikes from LPG neurons are
85 also found on the *pyn* nerve in these recordings, and can be differentiated from PY spikes by their
86 shape and their timing (LPG spikes during PD bursts). Under these control conditions, where the
87 rhythm is robust and spikes from these neurons are easily identifiable both by their location on the
88 nerve and their phase in the cycle, the dual problems of identifying spikes from raw extracellular
89 recordings and meaningfully describing circuit dynamics is easily resolvable.

90 In studies that characterize the changes in circuit dynamics to prolonged perturbations, spike
91 identification and circuit dynamics characterization is less straightforward. For example, when

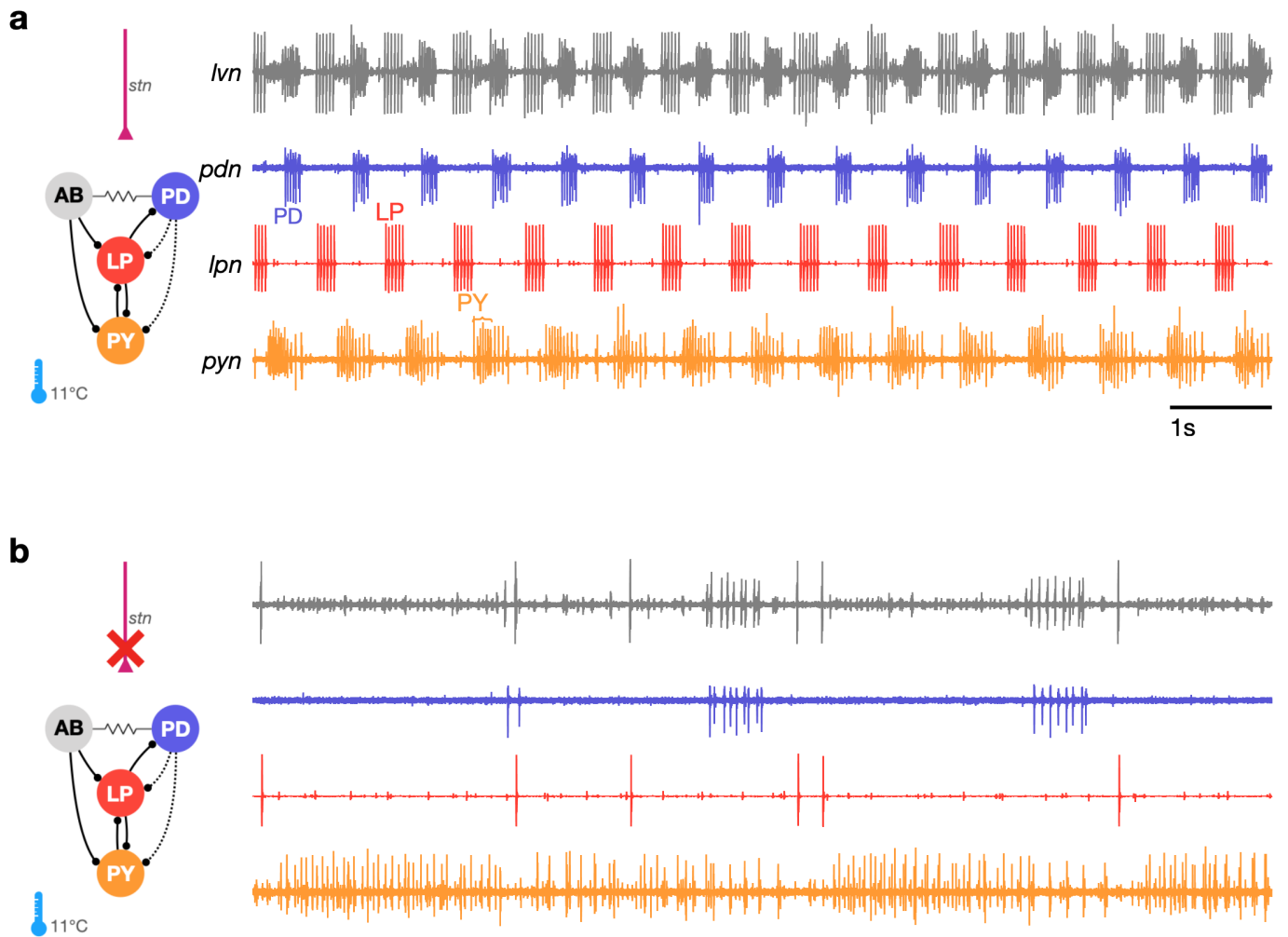


Figure 1. The triphasic pyloric rhythm can become irregular and hard to characterize under perturbation. (a) Simplified schematic of part of the pyloric circuit (left). Filled circles indicate inhibitory synapses. Solid lines are glutamatergic synapses and dotted lines are cholinergic synapses. Resistor symbol indicates electrical coupling. The pyloric circuit is subject to descending neuromodulatory control from the stomatogastric nerve (*stn*). (Right) simultaneous extracellular recordings from the *lvn*, *lpn*, *pdn* and *pyn* motor nerves. Action potentials from LP, PD and PY are visible on *lpn*, *pdn* and *pyn*. Under these baseline conditions, PD, LP and PY neurons burst in a triphasic pattern. The AB neuron is an endogenous burster and is electrically coupled to PD neurons. (b) When the *stn* is cut, neuromodulatory input is removed and the circuit is "decentralized". In this case, the pyloric rhythm can become irregular and hard to characterize. In addition, spikes from multiple PY neurons can become harder to reliably identify on *pyn*.

92 descending neuromodulatory projections from the *stn* are cut (i.e., when the STG is decentralized,
93 **Figure 1b**), the collective dynamics of the pyloric circuit can become less regular. This loss of
94 regularity is concomitant with spikes being harder to reliably identify in extracellular recordings.
95 While PD and LP neuron spikes can still be typically easily identified on the *pdn* and *lpn* nerves (
96 **Figure 1b**), identifying PY on the *pyn* in the absence of a regular rhythm can be challenging. This
97 problem is aggravated by the fact that spikes from the LPG neuron are frequently found on *pyn*,
98 and because there are several copies of the PY neuron, whose spikes can range from perfect
99 coincidence to slight offsets that can unpredictably change the amplitude and shape of PY spikes
100 due to partial summation. For these reasons, some previous work studying the response of pyloric
101 circuits to perturbations have consistently recorded from the *lpn* and *pdn* nerves, but not from the
102 *pyn* (**Hamood et al., 2015; Haley et al., 2018; Haddad and Marder, 2018; Rosenbaum and Marder,**
103 **2018**). Therefore, in order to include the largest number of experiments in our meta-analysis, we
104 chose to characterize the dynamics of the LP and PD neurons.

105 **Nonlinear dimensionality reduction allows for the visualization of diverse pyloric** 106 **circuit dynamics**

107 The regular pyloric rhythm involves out-of-phase bursts of spikes between LP and PD, and is
108 observed under baseline conditions (**Figure 2a1-3**). Perturbations such as the removal of descending
109 neuromodulatory inputs, changes in temperature, or changes in pH can qualitatively alter the
110 rhythm, leading to a large variety of hard-to-characterize spiking patterns (**Figure 2a4-6**). Because
111 these irregular states may lose the strong periodicity found in the canonical motor pattern, burst
112 metrics such as burst period or phase offsets between bursts that work well to characterize the
113 regular rhythm perform poorly. Efforts to characterize and quantify these atypical spike patterns
114 must overcome the slow timescales in observed dynamics, the large quantity of data, and irregularity
115 and variability in observed spike trains. Previous work used *ad-hoc* categorization systems to assign
116 observations of spike trains into one of a few groups (**Haddad and Marder, 2018; Haley et al., 2018**),
117 but these categorization methods scaled poorly and relied on subjective annotations.

118 We sought instead to visualize the totality of pyloric circuit dynamics under all conditions using
119 an unsupervised method that did not rely on *a-priori* identification of canonical dynamical patterns.
120 Such a data visualization method, while descriptive, would generate a quantitative vocabulary to
121 catalogue the diversity of spike patterns observed both when these patterns were regular and also
122 when they were irregular and aperiodic, thus allowing for the quantitative characterization of data
123 previously inaccessible to traditional methods (**Börner et al., 2003; Nguyen and Holmes, 2019**).

124 The visualization was generated as follows: time-binned (20s) spike trains were converted
125 into their equivalent inter-spike interval (ISI) and phase representations (**Figure 2b**, Methods and
126 Materials). Because there can be an arbitrary number of spikes in a bin, there are an arbitrary
127 number of ISIs and phases. To convert this into a vector of fixed length, we measured percentiles of
128 ISIs and phases (**Figure 2c**). Together with other metrics (Methods and Materials), these percentiles
129 were assembled into a fixed-length vector and each dimension was *z*-scored across the entire
130 dataset (**Figure 2d**). A collection of spike trains from an arbitrary number of neurons has thus been
131 reduced to a matrix where each row consists of *z*-scored percentiles of ISIs and other metrics. This
132 matrix can be visualized using a non-linear dimensionality reduction technique such as *t*-distributed
133 stochastic neighbor embedding (t-SNE) (**Van der Maaten and Hinton, 2008**), which can generate a
134 two-dimensional representation of the full data set (**Figure 2e**).

135 In this representation, each dot corresponds to a single time bin of spike trains from both
136 neurons. We found that spike trains that are visually similar (**Figure 2a1-3**) tend to occur close to
137 each other in the embedding (**Figure 2e1-3**). Spike patterns that are qualitatively different from each
138 other (**Figure 2a4-6**) tended to occur far from each other, often in clusters separated by regions of
139 low data density (**Figure 2e4-6**).

140 How useful is such a visualization and does it represent the variation in spike patterns in the data
141 in a reasonable manner? We colored each point by classically defined features such as the burst

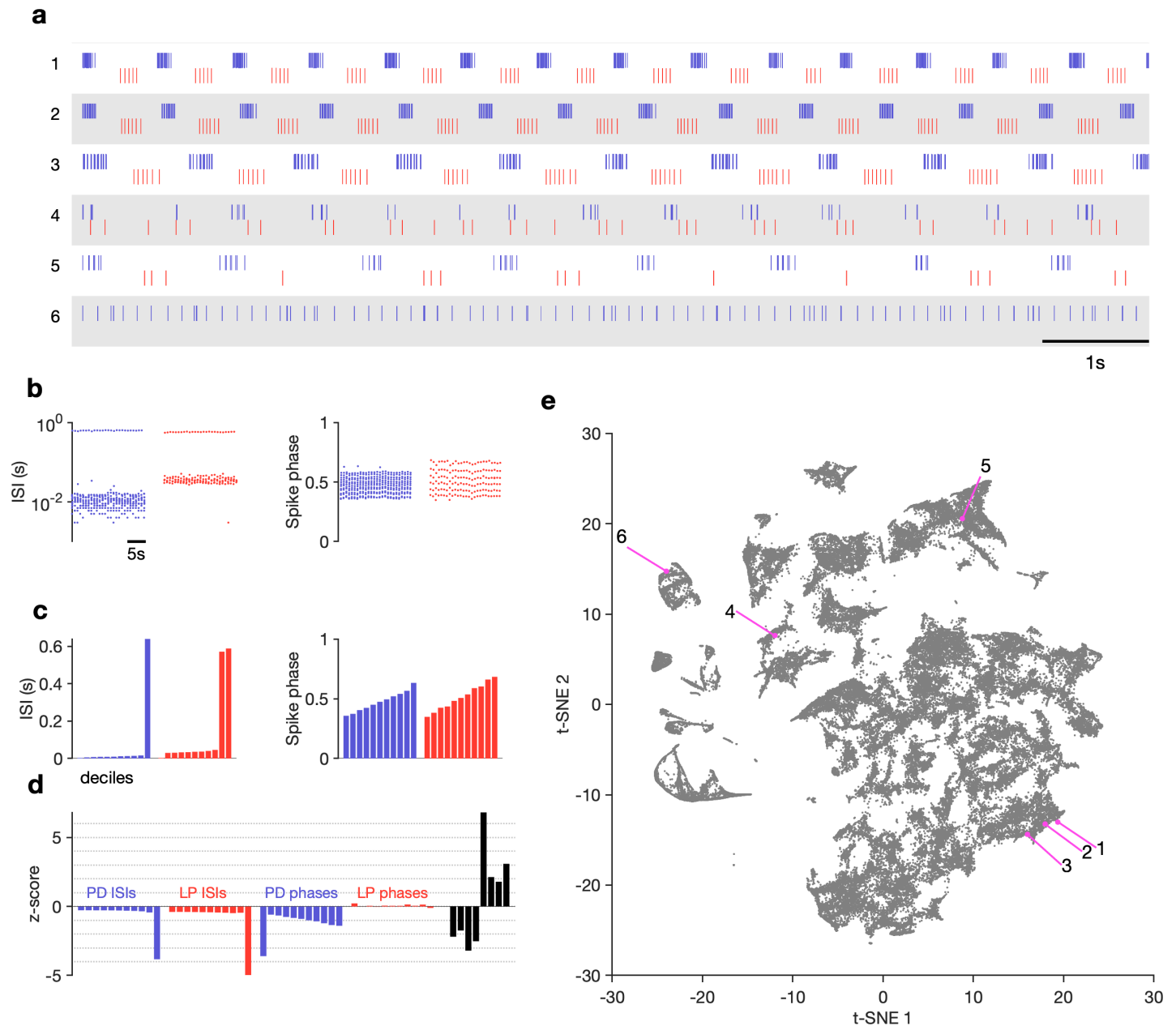


Figure 2. Visualization of diverse neural circuit dynamics. (a) Examples of canonical (1-3) and atypical (4-6) spike patterns of PD (blue) and LP (red). Rasters show 10s of data. (b-d) Schematic of data analysis pipeline. (b) Spike rasters in (a-2) can be equivalently represented by inter-spike intervals and phases. (c) Summary statistics of ISI and phase sets in (d), showing tenth-percentiles. (d) z-scored data assembled into a single vector, together with some additional measures (Methods and Materials). (e) Embedding of data matrix containing all vectors such as the one shown in (d) using t-SNE. Each dot in this image corresponds to a single 20-second spike train from both LP and PD. Example spike patterns shown in (a) are highlighted in the map. $n = 94844$ points from $N = 426$ animals. In (a-d), features derived from with LP spike times are shown in red, and features derived from PD spike times are shown in blue.

Figure 2-Figure supplement 1. Burst metrics smoothly vary in map.

Figure 2-Figure supplement 2. Embedding arranges data so that neighbors tend to be similar.

Figure 2-Figure supplement 3. Effect of varying perplexity in t-SNE embedding.

142 period or the phase (**Figure 2–Figure Supplement 1**). We found that the embedding arranges data so
143 that differences between clusters and within clusters had interpretable differences in various burst
144 metrics. For example, clusters on the left edge of the map tended not to have defined LP phases,
145 typically due to silent or very sparse LP firing (**Figure 2–Figure Supplement 1b**). Location of data in
146 the largest cluster was correlated to firing rate in the PD neuron (**Figure 2–Figure Supplement 1c**).
147 We observed that burst metrics, when they were defined, tended to vary smoothly across the map.
148 To quantify this observation, we built a Delaunay triangulation (Methods and Materials) on the
149 embedded data and measured the triadic differences between PD burst periods and PD duty cycles
150 (**Figure 2–Figure Supplement 2**). Triadic differences in these metrics were significantly smaller in
151 the map than triadic differences in a projection of the first two principal components or a shuffled
152 map ($p < .0001$, Kolmogorov-Smirnoff test), suggesting that the t-SNE cost function generates a
153 useful embedding where spike features vary smoothly within clusters.

154 Visualization of circuit dynamics allows manual labelling and clustering of data

155 Previous studies have shown that regular oscillatory bursting activity of the pyloric circuit can quali-
156 tatively change on perturbation. Circuit dynamics can be highly variable, and has been categorized
157 into various states such as "atypical firing", "LP-01 spikes" or "atypical" (**Haddad and Marder, 2018**;
158 **Haley et al., 2018**). Both the process of constructing these categories and the process of classifying
159 data into these categories are typically done manually, and therefore requires expert knowledge
160 that is not explicitly captured and is impossible to reproduce. Because the embedding distributed
161 data into clusters, we hypothesized that clusters corresponded to stereotyped dynamics that
162 were largely similar, and different clusters represented the qualitatively different circuit dynamics
163 identified by earlier studies.

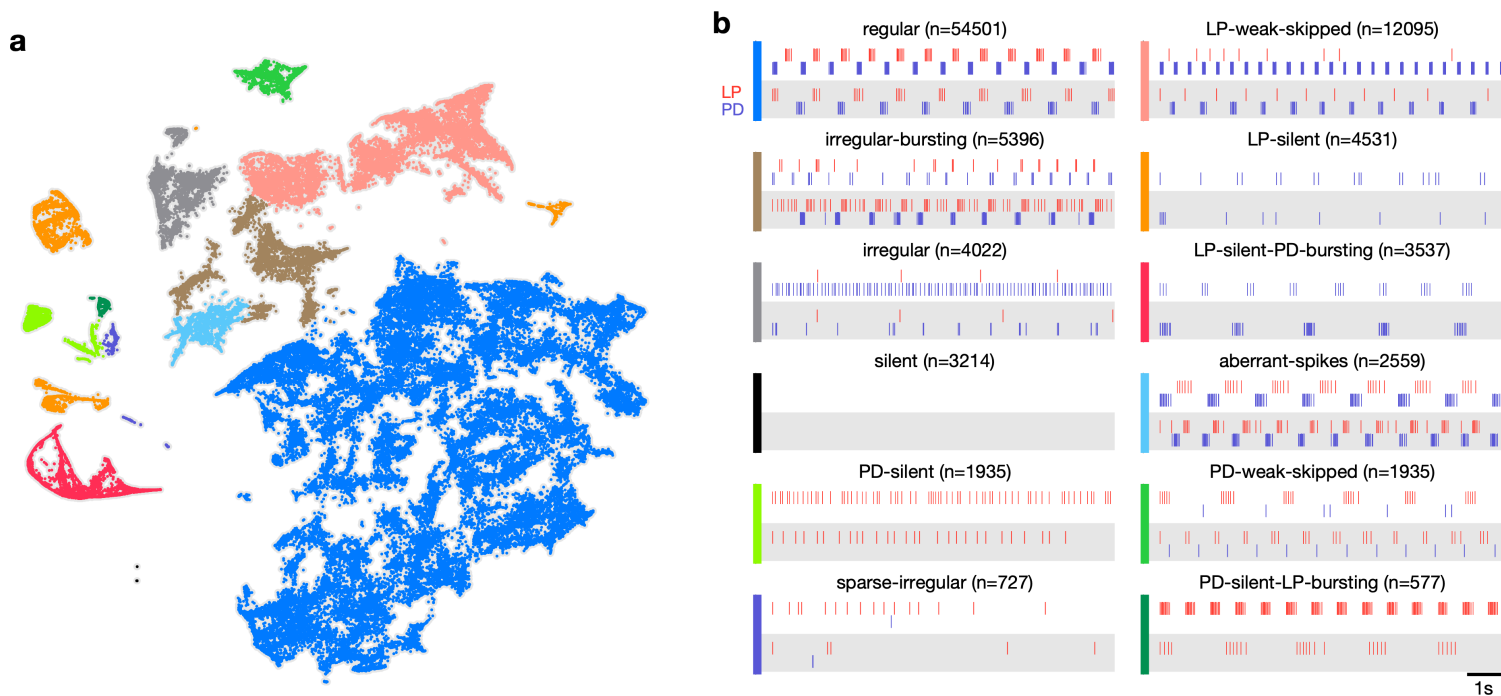


Figure 3. Map allows identification of distinct spiking dynamics. (a) Map of all pyloric dynamics in dataset where each point is colored by manually assigned labels. Each point corresponds to a 20s paired spike train from LP and PD. Each panel in (b) shows two randomly chosen points from that class. The number of points in each class is shown in parentheses above each panel. $n = 94844$ points from $N = 426$ animals. Labels are ordered by likelihood in the data.

Figure 3–Figure supplement 1. Speed of trajectories through map.

Figure 3–Figure supplement 2. Embeddings with different initializations.

164 We therefore inspected circuit dynamics at randomly chosen points in each apparent cluster,
165 and generated labels to describe the dynamics in that region (**Figure 3**). This process colored the
166 map and segmented it into distinct regions that broadly followed, and were largely determined by,
167 the distribution of the data in the embedding (**Figure 3a**). Most of the data (57%) were assigned
168 the `regular` label, where both PD and LP neurons burst regularly in alternation with at least two
169 spikes per burst, and all identified `regular` states occurred in a single contiguous region in the map
170 (blue). In the `LP-weak-skipped` state, PD bursts regularly, but LP does not burst every cycle, or only
171 fires a single spike per burst. `irregular-bursting` states showed bursting activity on both neurons,
172 which were interrupted or otherwise irregular. In contrast, the `irregular` state showed spiking that
173 was more variable, and did not show strong signs of bursting at any point. `LP-silent-PD-bursting`
174 states had regular bursting on PD, with no spikes on LP, while `LP-silent` states also had no spikes
175 on LP, but activity on PD was more variable, and did not show regular bursting.

176 The time evolution of the pyloric dynamics of every preparation constitutes a trajectory in the
177 map, and every point in the map is therefore associated with an instantaneous speed of motion
178 in the map. We hypothesized that instantaneous speed could vary across the map, with points
179 labelled `regular` moving more slowly through the map than points with labels corresponding to
180 atypical states such as `irregular`, because `regular` rhythms would vary less over time. Consistent
181 with this, we found that points in the `regular` cluster tended to have smaller speeds than points
182 in other clusters (**Figure 3-Figure Supplement 1a**). Speeds in the `regular` state were significantly
183 lower than every other state except `PD-silent-LP-bursting` ($p < .004$, permutation test), suggesting
184 that atypical states were associated with increased variability in circuit dynamics (**Figure 3-Figure
185 Supplement 1b**).

186 **Variability in baseline circuit dynamics across a population of wild-caught animals**

187 Work on the pyloric circuit has almost exclusively used a wild-caught crustacean population. This
188 uncontrolled environmental and genetic variability serves as a window into the extant variability
189 of a functional neural circuit in a wild population of animals. In addition, experimental and
190 computational work has shown that similar rhythms can be generated by a wide variety of circuit
191 architectures and cellular parameters (*Prinz et al., 2003; Hamood and Marder, 2015; Alonso and
192 Marder, 2019*). We therefore set out to study the variability in baseline circuit dynamics in the 346
193 pyloric circuits recorded from under baseline conditions in this dataset.

194 The burst period of the pyloric circuit in the lobster can vary 2-3 fold under baseline conditions
195 at 11°C across animals (*Bucher et al., 2005*). Despite this sizable variation, other burst metrics,
196 such as the phase onset of follower neurons, or the duty cycles of individual neurons, are tightly
197 constrained (*Bucher et al., 2005*), likely related to the fact that these circuits are under activity-
198 dependent feedback regulation (*Turrigiano et al., 1995; O'Leary et al., 2014; Gorur-Shandilya et al.,
199 2020*) as they develop and grow. Activity-dependent regulation of diverse pyloric circuits could
200 constrain variability in a single circuit across time to be smaller than variability across the population.

201 To test this hypothesis, we measured a number of burst metrics such as burst period and the
202 phases and duty cycles of the two neurons across these 346 preparations in baseline conditions
203 (**Figure 4**) when data are labelled `regular`, because metrics are well-defined in this state. Mean
204 values of each of these metrics were unimodally distributed (**Figure 4a**) and the coefficient of
205 variation for all metrics was approximately 0.1 (**Figure 4b**). Using the mean coefficient of variation
206 in each individual as a proxy for the within-animal variability, and the coefficient of variation of the
207 individual means as a proxy for the across-animal variability, we found that every metric measured
208 was more variable across animals than within animals (**Figure 4c**). Shuffling experimental labels
209 generated null distributions for excess variability across animals, and showed that across animal
210 variability was significantly greater than within animal variability (**Figure 4d**, $p < .007$, permutation
211 test, Table 1).

212 It is reasonable to suppose that all baseline data exist in the `regular` cluster. While most baseline
213 data are confined to the `regular` cluster ($\approx 80\%$, **Figure 4-Figure Supplement 1a**), the remaining

214 data, nominally recorded under baseline conditions, contains atypical circuit dynamics (**Figure 4–**
 215 **Figure Supplement 1b-c**). What causes these atypical circuit dynamics in this large, unbiased survey
 216 of baseline pyloric activity? One possibility could be inadvertent damage to the preparation caused
 217 by dissection and preparation of the circuit for recording. Consistent with this, we found that the
 218 probability of observing `regular` states was significantly reduced when cells were recorded from
 219 intracellularly (**Figure 4–Figure Supplement 2**), which may be due to increase in leak currents due
 220 to impaling cells with sharp electrodes (Cymbalyuk *et al.*, 2002), or due to cell dialysis (Hooper
 221 *et al.*, 2015). No significant correlation was observed between sea surface temperatures (a proxy
 222 for environmental conditions for these wild-caught animals) and burst metrics (**Figure 4–Figure**
 223 **Supplement 4a-c**) or the probability of observing a `regular` state (**Figure 4–Figure Supplement 4d**).
 224 Taken together, these results underscore the importance of verifying that baseline or control data
 225 does not include uncontrolled technical variability that could mask biological effects of interest.

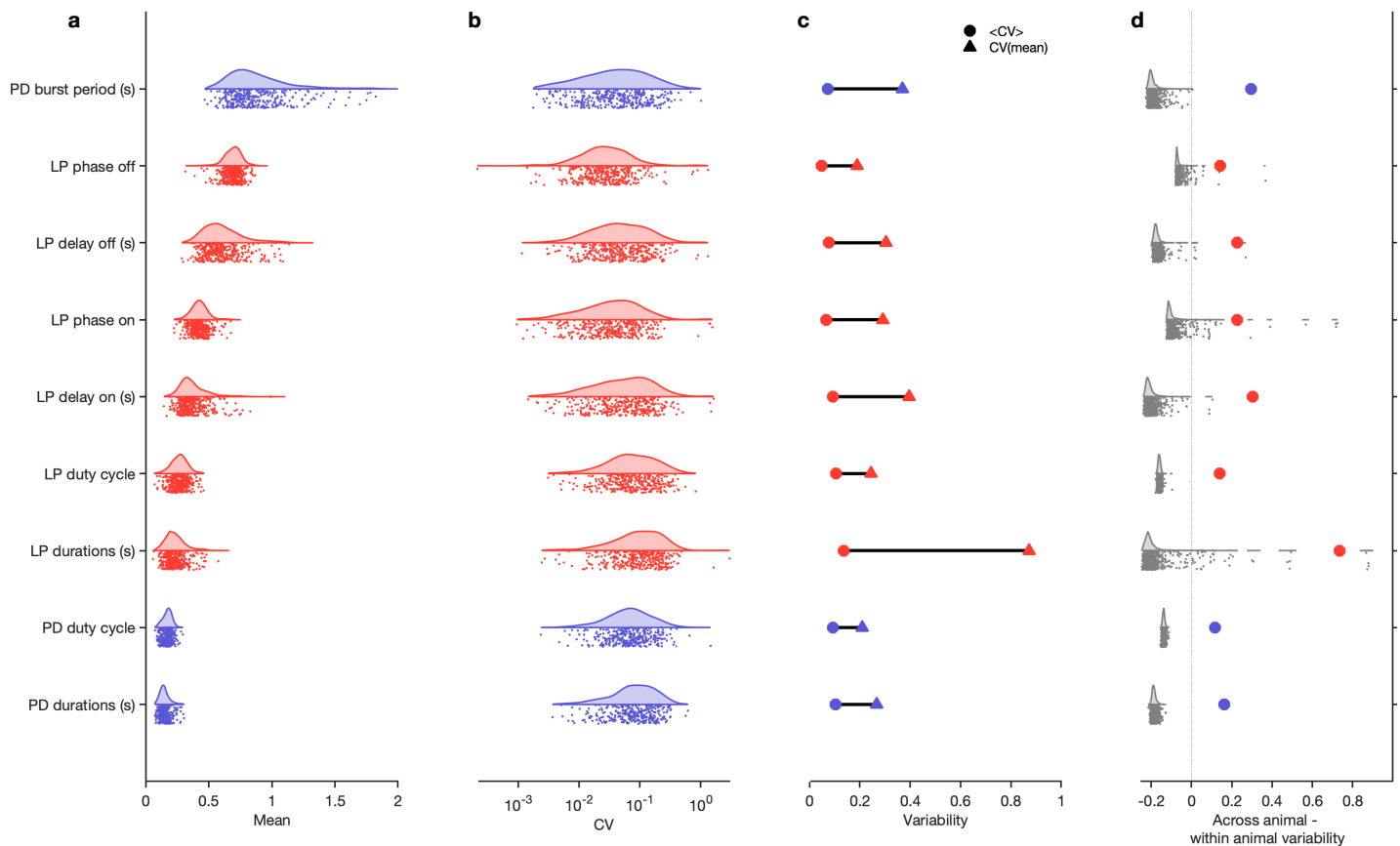


Figure 4. Variability of burst metrics under baseline conditions. (a) Variability of burst metrics in PD and LP neurons across a population of wild caught animals. Metrics are only computed under baseline conditions and in the `regular` cluster. (b) Distribution of coefficient of variation (CV) of metrics in each animal across all data from that animal. In (a-b), each dot is from a single animal, and distributions show variability across the entire population. (c) Across-animal variability (CV of individual means, Δ) is greater than within-animal variation (mean of CV in each animal, \circ) for every metric. (d) Difference between across animal variability and within animal variability (colored dots). For each metric, gray dots and distribution show differences between across-animal and within-animal variability for shuffled data. $n = 18336$ points from $N = 346$ animals.

Figure 4–Figure supplement 1. State distribution under baseline conditions

Figure 4–Figure supplement 2. Recording condition alters `regular` state probability

Figure 4–Figure supplement 3. Effect of sea surface temperature on baseline circuit dynamics

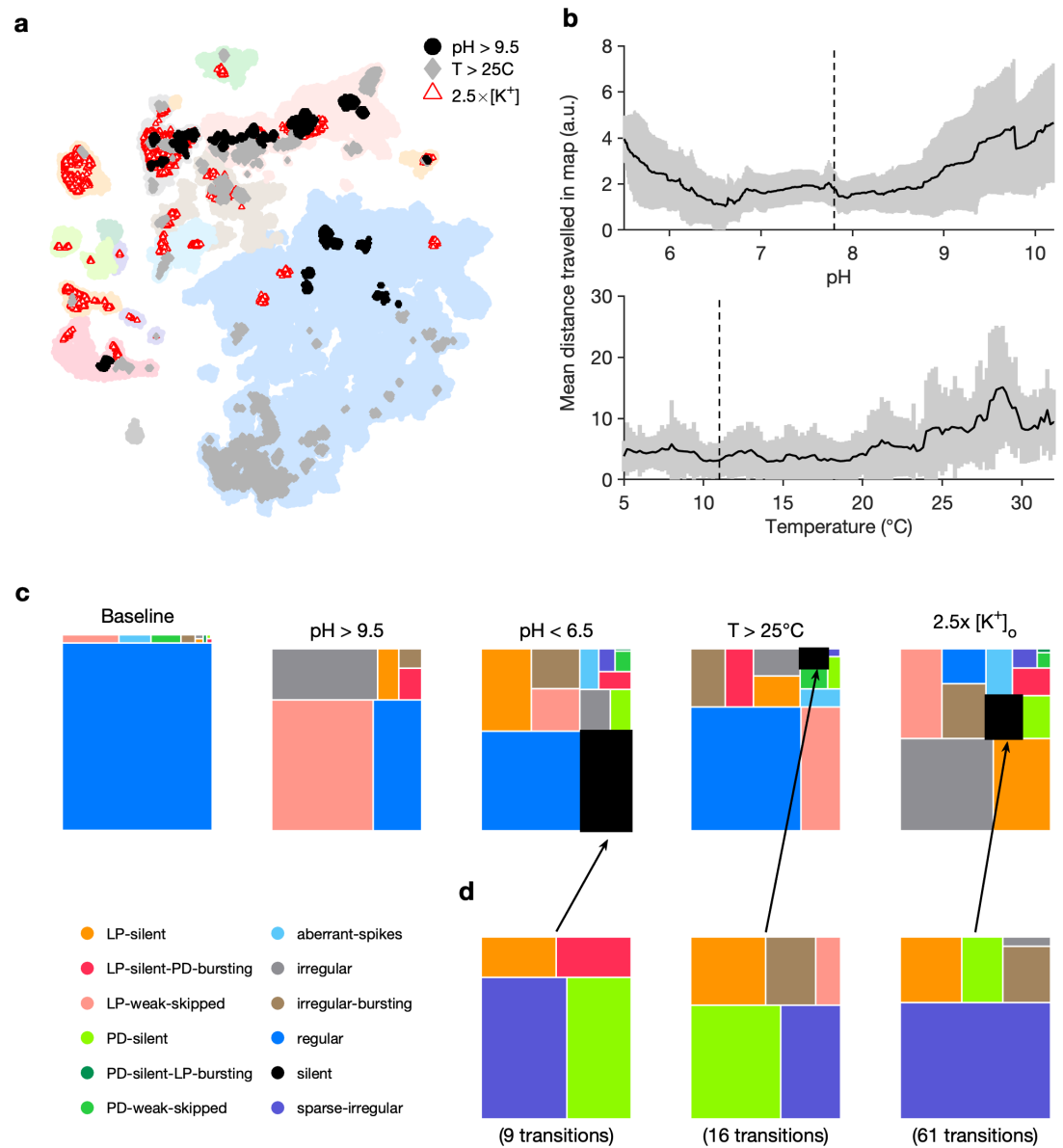


Figure 5. Effect of three different environmental perturbations. (a) Map showing regions that are more likely to contain data recorded under extreme environmental perturbations. (b) Mean distance travelled in map during pH and temperature perturbations. Solid lines indicate mean and shading is the standard deviation across all preparations. Vertical dashed lines indicate baseline conditions. (c) Treemaps showing probability distributions of states under baseline and perturbed conditions. (d) Probability distribution of states preceding silent state under perturbation. pH perturbations: $n = 4023$ from 6 animals. [K⁺] perturbations: $n = 5526$ from 20 animals. Temperature perturbations: $n = 80470$ from 414 animals.

Figure 5-Figure supplement 1. Preparation-by-preparation response to pH perturbations.

Table 1. ANOVA results and power analysis for *Figure 4*

Metric	Across animal MS	Within animal MS	F	$N_{.99}$
LP delay off (s)	1.1391	0.010956	103.97	6
LP delay on (s)	0.61647	0.0111	55.54	6
LP durations (s)	0.36386	0.012366	29.424	4
LP duty cycle	0.15986	0.0013093	122.09	10
LP phase off	0.23406	0.0072279	32.383	11
LP phase on	0.21655	0.0088115	24.576	9
PD burst period (s)	3.557	0.036872	96.469	4
PD durations (s)	0.079397	0.00054944	144.5	6
PD duty cycle	0.053472	0.00041323	129.4	16

Table 1—source data 1. ANOVA results for burst metrics in baseline conditions. For each metric, each animal is treated as a group and the variability (mean square difference) is compared within and across group. F is the ratio of across-animal to within-animal mean square differences. $N_{.99}$ is the estimate of the sample size required to reject the null hypothesis with a probability of .99 when the alternative hypothesis is true. $N = 346$ animals.

226 **Perturbation modality alters state probability**

227 The pyloric circuit and other circuits in the crab must exhibit robustness to the environmental
228 perturbations that these animals are likely to encounter. Previous studies have characterized the
229 ability of crustacean circuits to be robust to environmental perturbations such as pH (*Haley et al.,*
230 *2018; Ratliff et al., 2021; Qadri et al., 2007*), temperature (*Tang et al., 2010, 2012; Rinberg et al.,*
231 *2013; Haddad and Marder, 2018; Kushinsky et al., 2019*), oxygen levels (*Clemens et al., 2001*) and
232 changes in extracellular ionic concentrations (*He et al., 2020*). Robustness to these perturbations
233 exists up to a limit, likely reflecting the bounds of the natural variation in these quantities that these
234 circuits are evolved to function in. When challenged with extremes of any of these perturbation
235 modalities, the pyloric rhythm breaks down, displaying irregular or aberrant states, and may even
236 cease spiking entirely.

237 What remains unclear is if extreme perturbations of different modalities share common path-
238 ways of destabilizing and disrupting the pyloric rhythm (*Ratliff et al., 2021*). In principle, these
239 environmental perturbations can disrupt neuron and circuit function in qualitatively different ways:
240 e.g., changes in extracellular potassium concentration can alter the reversal potential of potassium
241 (*He et al., 2020*) vs. changes in temperature can have varied effects on the timescales and conduc-
242 tances of all ion channels (*Tang et al., 2010; Caplan et al., 2014*). Because prior work was focussed
243 on studying the limits of robustness, and lacked a detailed quantitative description of irregular
244 behavior, the fine structure of the transition between functional dynamics and silent or "crashed"
245 states remain poorly characterized (*Ratliff et al., 2021*). We therefore set out to measure how pH,
246 temperature and extracellular potassium perturbations alter circuit state probability.

247 Where in the map are data under extreme environmental perturbations? Circuit spike patterns
248 under high pH (>9.5), high temperature (>25°C) and high extracellular potassium ($2.5 \times [K^+]$) are
249 distributed across a wide region of the map, spanning both regions in the `regular` cluster and
250 other non-regular clusters (*Figure 5a*). Spike patterns observed under high temperature conditions
251 in the `regular` region were clustered in the lower extremity, in the region containing high firing
252 rates and small burst periods of PD (*Figure 2–Figure Supplement 1*), consistent with earlier studies
253 showing that elevated temperatures tend to speed up the pyloric rhythm (*Tang et al., 2010, 2012*).
254 To characterize how environmental perturbations destabilize the pyloric rhythm and increase the
255 variability in observed dynamics, we measured the mean distance travelled in the map by each
256 preparation as a function of the perturbation intensity (*Figure 5b*). For both pH and temperature
257 perturbations, the mean distance travelled in the map was lowest at baseline conditions (pH

258 7.8, 11°C) and increased away from these conditions, suggesting that changes in either of these
259 environmental parameters increased the variability in observed pyloric dynamics ($\rho = .95$ for $\text{pH} > 7.8$,
260 $\rho = -.36$ for $\text{pH} < 7.8$, $\rho = .81$ for $T > 11^\circ\text{C}$, $p < .001$, Spearman rank correlation test).

261 Subjecting the pyloric circuit to extremes of pH, temperature and extracellular potassium altered
262 the distribution of observed states (**Figure 5c**). In all cases, the probability of observing `regular`
263 was significantly reduced ($p < .001$, paired permutation test), and a variety of non-regular states
264 were observed. We observed that high pH (> 9.5) did not silence the preparation, but silent states
265 were observed in low pH (< 6.5), consistent with previously published manual annotation of this
266 data (**Haley et al., 2018**). Silent states were also observed in $2.5 \times [K^+]$, as reported earlier by **He**
267 **et al. (2020)**. Previous work has shown that the isolated pacemaker kernel (AB and PD neurons)
268 has a stereotyped trajectory from bursting through tonic spiking to silence when subjected to
269 temperature and high $[K^+]$ perturbations (**Ratliff et al., 2021**). Do pathways to silent states share
270 similarities across perturbation modality in intact circuits? To answer this, we plotted the probability
271 of observing states conditioned on the transition to silence in low pH, high temperature, and
272 $2.5 \times [K^+]$ (**Figure 5d**). In the ≈ 2000 transitions between states detected, we never observed a
273 transition from `regular` to `silent`, suggesting that the timescales of silencing are slow, longer
274 than the width of one data bin (20s). Trajectories to `silent` states always transition through a few
275 intermediate states such as `sparse-irregular`, `LP-silent` or `PD-silent` (**Figure 5d**).

276 **Transitions between states during environmental perturbations**

277 Changes in temperature, pH and $[K^+]$ have different effects on the cells in the pyloric circuit and
278 therefore can destabilize the rhythm in different ways. Increasing the extracellular $[K^+]$ changes
279 the reversal potential of K^+ ions, altering the currents flowing through potassium channels, and
280 typically depolarizes the neuron (**He et al., 2020**). Ion channels can be differentially sensitive to
281 changes in temperature or pH, and changes in these variables can have complex effects of ionic
282 currents in neurons (**Tang et al., 2010, 2012; Haley et al., 2018**). We therefore asked if different
283 environmental perturbations changed the way in which `regular` rhythms destabilized.

284 Our analysis mapped a time series of spiketimes from PD and LP neurons to a categorical time
285 series of labels such as `regular`. We therefore could measure the transitions between states during
286 different environmental perturbations (Methods and Materials). We found that transition matrices
287 between states shared commonalities across environmental perturbations (**Figure 6a**), such as likely
288 transitions between `regular` and `LP-weak-skipped` states. `PD-silent`-`LP-bursting` states tended
289 to be followed by `PD-silent` states, in which the LP neuron is spiking, but not bursting regularly.
290 The LP neuron becomes less regular in both transitions, contributing to the loss of regular rhythms.
291 We never observed a transition from `regular` rhythms `LP-silent` or `PD-silent` states, suggesting
292 slow ($> 20\text{s}$) timescales of rhythm collapse. In high pH, every transition away from the `regular` state
293 was to the `LP-weak-skipped` state, hinting at increased sensitivity of the LP neuron to high pH. High
294 pH perturbations also never silenced the circuit, as previously reported (**Haley et al., 2018**), and
295 showed fewer and less varied transitions than other perturbations. Are some transitions over-
296 or under-represented in the transition matrix? To determine this, we constructed a null model
297 where transitions occurred with probabilities that scaled with the marginal probability of final states
298 (Methods and Materials). Transitions that occurred significantly more often than predicted by the
299 null model are shown with black borders and those that occurred significantly less often than
300 predicted are shown with filled circles (**Figure 6a**). Transitions that never occurred, but occurred at
301 significantly non-zero rates in the null model are indicated with diamonds.

302 Earlier work has shown that transitions from regular bursting are preceded by an increase in
303 variability in the voltage dynamics of bursting in PD neurons pharmacologically isolated from most
304 of the pyloric circuit (**Ratliff et al., 2021**). Can we detect similar signatures of destabilization before
305 transitions from `regular` states in the intact circuit? We measure the coefficient of variation (CV)
306 of the burst periods of PD and LP neurons in `regular` states just before transitions away from
307 `regular` (**Figure 6b**). Because we restricted our measurement of variability to `regular` states, we

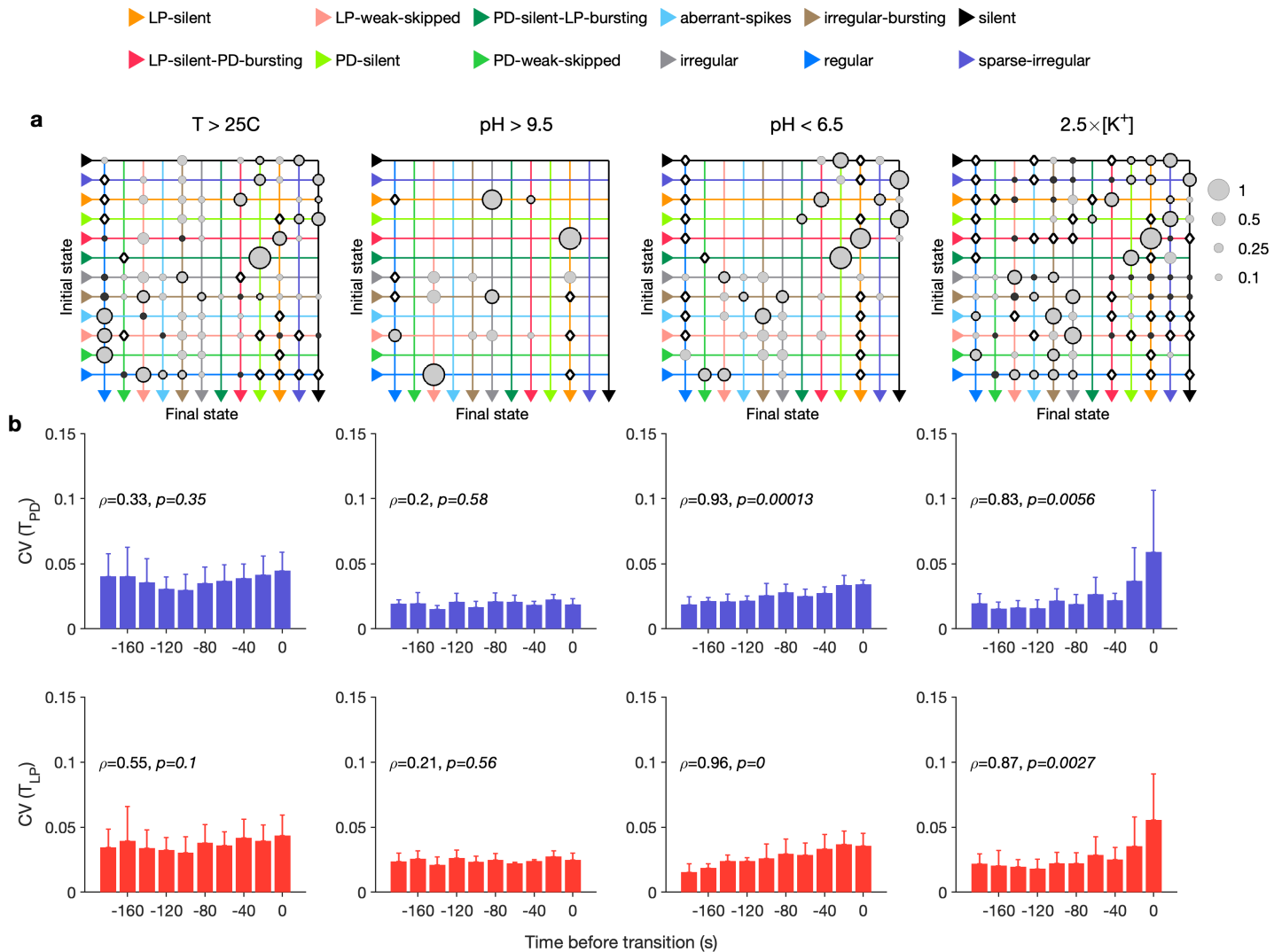


Figure 6. Effect of environmental perturbations on transitions between states. (a) Transition matrix between states during environmental perturbations. Each matrix shows the conditional probability of observing the final state in the next time step given an observation of the initial state. Probabilities in each row sum to 1. Size of disc scales with probability. Discs with dark borders are transitions that are significantly more likely than the null model (Methods and Materials). Dark solid discs are transitions with non-zero probability that are significantly less likely than in the null model. \diamond are transitions that are never observed, and are significantly less likely than in the null model. States are ordered from regular to silent. (b) Coefficient of variation (CV) of burst period of PD (purple) and LP (red) vs. time before transition away from the regular state. ρ , p are from Spearman test to check if variability increases significantly before transition. Temperature perturbations: $n = 1035$ transitions in 61 animals. pH perturbations: $n = 90$ transitions in 6 animals. $[K^+]$ perturbations: $n = 271$ transitions in 20 animals.

308 could disambiguate true cycle-to-cycle jitter in the timing of bursts from the apparent variability
309 in cycle period due to alternations between bursting and non-bursting dynamics. We found that
310 transitions away from `regular` were correlated with a steady and almost monotonic increase in
311 variability in PD and LP burst periods for low pH and high $[K^+]$ perturbations, but not for high pH
312 and high temperature perturbations (Spearman rank correlation test). This suggests mechanistically
313 different underpinnings to the pathways of destabilization between these sets of perturbations, and
314 is consistent with previous work showing that robustness to perturbations in pH only moderately
315 affects temperature robustness in the same neuron (Ratliff et al., 2021).

316 **Decentralization elicits variable circuit dynamics**

317 The pyloric circuit is modulated by a large and chemically diverse family of neuromodulators that
318 it receives via the stomatogastric (*stn*) nerve (Marder, 2012). Decentralization, or the removal of
319 this neuromodulatory input via transection and/or chemical block of the *stn*, has been shown
320 to affect the pyloric rhythm in a number of ways (Russell, 1976). Decentralization can stop the
321 rhythm temporarily, which can recover after a few days (Golowasch et al., 1999; Thoby-Brisson
322 and Simmers, 1998). Decentralization slows down the pyloric rhythm (Eisen and Marder, 1982;
323 Rosenbaum and Marder, 2018), and makes the rhythm more variable (Hamood and Marder, 2015;
324 Hamood et al., 2015). Decentralization can evoke variable circuit dynamics, sometimes with slow
325 timescales (Figure 7–Figure Supplement 1), and can lead to changes in ion channel expression
326 (Mizrahi et al., 2001).

327 The variability in circuit dynamics elicited by decentralization, and the animal-to-animal variability
328 in response to decentralization has made a quantitative analysis of the effects of decentralization
329 difficult. We therefore set about to characterize the variable and invariant features of the changes
330 in circuit spiking dynamics on removal of descending neuromodulation across a large ($N = 141$)
331 population.

332 We first asked where in the map decentralized data were (Figure 7a). A large fraction ($\approx 30\%$)
333 of the data was found outside the `regular` cluster, suggesting the existence of atypical circuit
334 dynamics on decentralization. To determine if decentralization dispersed data in the map, and
335 made circuit dynamics more variable across time, we measured the mean distance travelled by each
336 preparation before and after decentralization (Figure 7b, Methods and Materials). Decentralization
337 significantly increased the distance covered by each preparation across the map ($p < .0001$, paired
338 permutation test), suggesting that circuits displayed more variable dynamics on decentralization.
339 Decentralization also changed probabilities of observing many states. The `regular` state was
340 significantly less likely on decentralization, and several atypical states were significantly more likely
341 (Figure 7c,d, Table 2, Figure 7–Figure Supplement 2).

342 How do preparations switch between different states when decentralized? The transition matrix
343 during decentralization revealed many transitions between diverse states (Figure 7e), with the most
344 likely transitions being significantly over-represented compared to the null model ($p < .05$, Methods
345 and Materials). Transitions away from `regular` included significantly more likely transitions into
346 states where one of the neurons was irregular such as `LP-weak-skipped` and `PD-weak-skipped`.
347 Similar to rhythm destabilization in high $[K^+]$ or low pH, transitions away from `regular` were
348 associated with a near-monotonic increase in the variability of PD and LP burst periods before the
349 transitions (Figure 7f, $\rho \approx .8$, $p < .006$, Spearman rank correlation test).

350 The time series of identified states on a preparation-by-preparation basis showed striking
351 variability in the responses to decentralization (Figure 7–Figure Supplement 3a), with the proba-
352 bility of observing `regular` states decreasing immediately after decentralization (Figure 7–Figure
353 Supplement 3b). What causes the observed animal-to-animal variability in circuit dynamics on
354 decentralization? One possibility is that seasonal changes in environmental conditions alter the
355 sensitivity of the pyloric circuit to neuromodulation. We tested this hypothesis by measuring the
356 correlation between measures such as the probability of observing the `regular` state, the change in
357 burst period, and the change in firing rate on decentralization and the sea surface temperature at

358 the approximate location of these wild caught animals (**Figure 7–Figure Supplement 4**). None of
 359 these measures was significantly correlated with sea surface temperature ($p > .07$, Spearman rank
 360 correlation test).

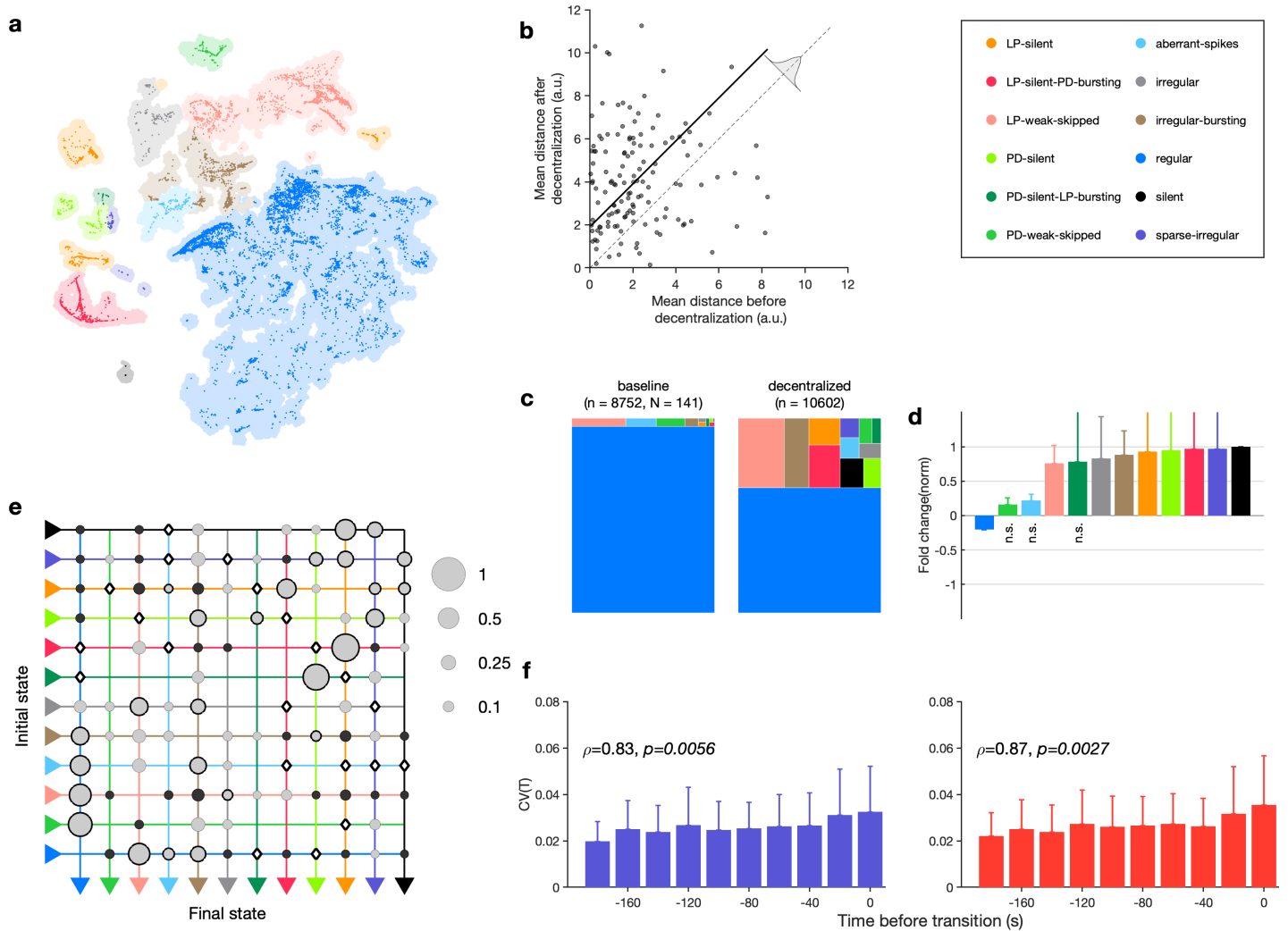


Figure 7. Effect of decentralization. (a) Map occupancy conditional on decentralization. Shading shows all data, bright colored dots indicate data when preparations are decentralized. (b) Distance travelled in map before and after decentralization. Each dot is a single preparation. Gray shading indicates null distribution and solid line is the mean difference upon decentralization. (c) State probabilities before and after decentralization. (d) Fold change in state probabilities on decentralization. States marked n.s. are not significantly more or less likely after decentralization. All other states are (paired permutation test, $p < 0.00016$). (a-b) $n = 10602$ points from $N = 141$ animals. (e) Transition matrix during decentralization. Probabilities in each row sum to 1. Size of disc scales with probability. Discs with dark borders are transitions that are significantly more likely than the null model (Methods and Materials). Dark solid discs are transitions with non-zero probability that are significantly less likely than in the null model. \diamond are transitions that are never observed, and are significantly less likely than in the null model. States are ordered from *regular* to *silent*. $n = 1933$ transitions. (f) Coefficient of variation of PD (purple) and LP (red) burst periods before transition away from *regular* states. ρ, p from Spearman test. $n = 1332$ points from $N = 79$ animals.

Figure 7–Figure supplement 1. Decentralization evokes variable dynamics

Figure 7–Figure supplement 2. Effects of decentralization on state probabilities

Figure 7–Figure supplement 3. Time course of effects of decentralization

Figure 7–Figure supplement 4. Effects of decentralization do not correlate with seasonal effects

Table 2. State counts before and after decentralization for data shown in *Figure 7*

State	$n_{control}$	$n_{dec.}$	p	$\Delta P(state)$
regular	7967	5791	<0.001	-0.308 77
LP-silent	22	724	<0.001	0.030 65
LP-silent-PD-bursting	14	577	<0.001	0.045 926
PD-silent	11	140	4×10^{-5}	0.018 51
PD-silent-LP-bursting	20	18	0.469 59	0.000 188 91
aberrant-spikes	111	168	0.300 37	0.003 285 3
LP-weak-skipped	317	1628	<0.001	0.099 875
PD-weak-skipped	142	118	0.292 19	0.003 453 8
sparse-irregular	4	154	<0.001	0.013 263
irregular	13	116	0.000 23	0.010 877
silent	0	321	<0.001	0.024 825
irregular-bursting	72	753	<0.001	0.057 913

Table 2-source data 1. State counts before and after decentralization. p -value of change in probability of observing change estimated from paired permutation tests.

361 **Stereotyped effects of decentralization on burst metrics**

362 Despite the animal-to-animal variation in responses to decentralization, are there stereotyped
 363 responses to decentralization? Previous work has shown that decentralization typically slows
 364 down the pyloric rhythm (*Eisen and Marder, 1982; Rosenbaum and Marder, 2018*), but a finer-
 365 grained analysis of rhythm metrics were confounded by the irregular dynamics that can arise
 366 when preparations are decentralized. For example, alteration between `regular` and atypical states
 367 could bias estimates of burst metrics that are not defined in atypical states. Because our analysis
 368 allows us to identify the subset of data where pyloric circuit dynamics are regular enough that
 369 burst metrics are well-defined, we measured the changes in a number of burst metrics like the
 370 burst period, duty cycle and phases on decentralization (*Figure 8a*). Every metric measured was
 371 significantly changed except the phase at which LP bursts start ($p < 0.007$, paired permutation test).
 372 Consistent with earlier studies, we found that the coefficient of variation in every metric increased
 373 following decentralization (*Figure 8b*).

374 What are the dynamics of changes in burst metrics on decentralization? Firing rates of both LP
 375 and PD neurons decreased immediately on decentralization, roughly halving their pre-decentralized
 376 values (*Figure 8c*). This occurred together with a doubling of PD burst periods (*Figure 8d*), suggesting
 377 that the entire rhythm is slowing down. Intriguingly, decentralization led to significant advance in
 378 the phase of LP burst ends, but not starts (*Figure 8e*), leading to a large decrease in the duty cycle of
 379 the LP neuron (*Figure 8f*) that was significantly more than the decrease in PD's duty cycle ($p < 10^{-8}$,
 380 paired t -test).

381 The stereotyped slowing of the rhythm on decentralization can also be quantified by looking
 382 at the distribution of the data in the `regular` cluster before and after decentralization (*Figure 8-
 383 Figure Supplement 1*). Data are concentrated in the upper left edge of the `regular` cluster when
 384 decentralized, where burst periods are large and firing rates low (*Figure 2-Figure Supplement 1a,c*),
 385 suggesting that decentralization could elicit a more stereotyped rhythm for circuits that continue
 386 to burst regularly, because circuits that do so tend to share a common, slow bursting dynamics.
 387 Counter-intuitively, it may appear that `regular` rhythms in baseline conditions are more variable
 388 than `regular` rhythms after decentralization. To test this hypothesis we measured the dispersion
 389 of each preparation in the map (*Figure 8-Figure Supplement 1b*) before and after decentralization.
 390 Dynamics before decentralization were significantly more dispersed in the `regular` cluster than
 391 dynamics after decentralization (*Figure 8-Figure Supplement 1c*, $p = .0016$, paired t -test), because
 392 they then tended to be concentrated in the upper-left edge of that cluster. To first approximation,

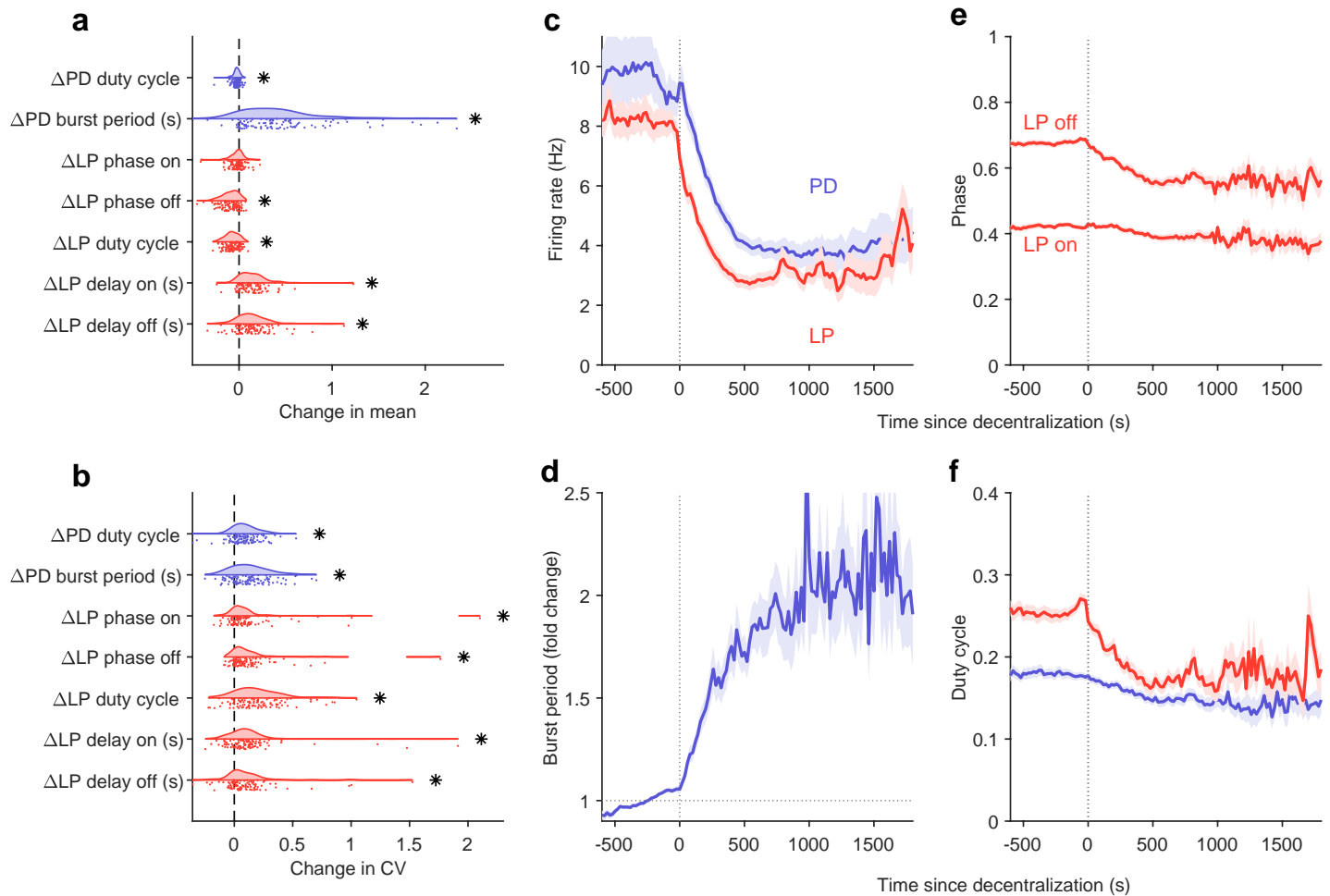


Figure 8. Effects of decentralization on burst metrics. (a) Change in mean burst metrics on decentralization. (b) Change in coefficient of variation of burst metrics on decentralization. In (a) and (b), each dot is a single preparation; * indicate distributions whose mean is significantly different from zero ($p < .007$, paired permutation test). Firing rates (c), burst period (d), LP phases (e) and duty cycles (f) vs. time since decentralization. In panels (c-f), thick lines indicate population means, and shading indicates the standard error of the mean. $n = 13898$ points from $N = 141$ preparations.

Figure 8-Figure supplement 1. Effects of decentralization on regular rhythms

393 our analysis shows that there are many ways to manifest a regular rhythm under baseline conditions,
 394 but regular rhythms on decentralization are typically slow, and stereotyped in comparison.

395 Neuromodulators differentially affect state probabilities

396 The crustacean stomatogastric ganglion is modulated by more than 30 substances (*Harris-Warrick*
 397 *and Marder, 1991; Marder, 2012*) that tune neuronal properties on an intermediate time scale,
 398 between feedback homeostasis and intrinsic cellular properties (*Daur et al., 2016*). Earlier work has
 399 focussed on understanding the effect modulators have on restoring (or destabilizing) the canonical
 400 rhythm, in part because the restoration of regular oscillatory dynamics is a dominant feature of
 401 neuromodulator action. Other effects that neuromodulators might have on pyloric circuit dynamics
 402 are harder to investigate, and are hindered by the difficulty in characterizing circuit dynamics when
 403 non-regular. Here we set out to systematically characterize the effects of neuromodulators on
 404 dynamical states identified in the full space of circuit behaviors (*Figure 3*).

405 We focussed our analysis on the effect of four neuromodulators: Red pigment-concentrating
 406 hormone (RPCH), proctolin, oxotremorine, and serotonin. In the experiments analyzed, these

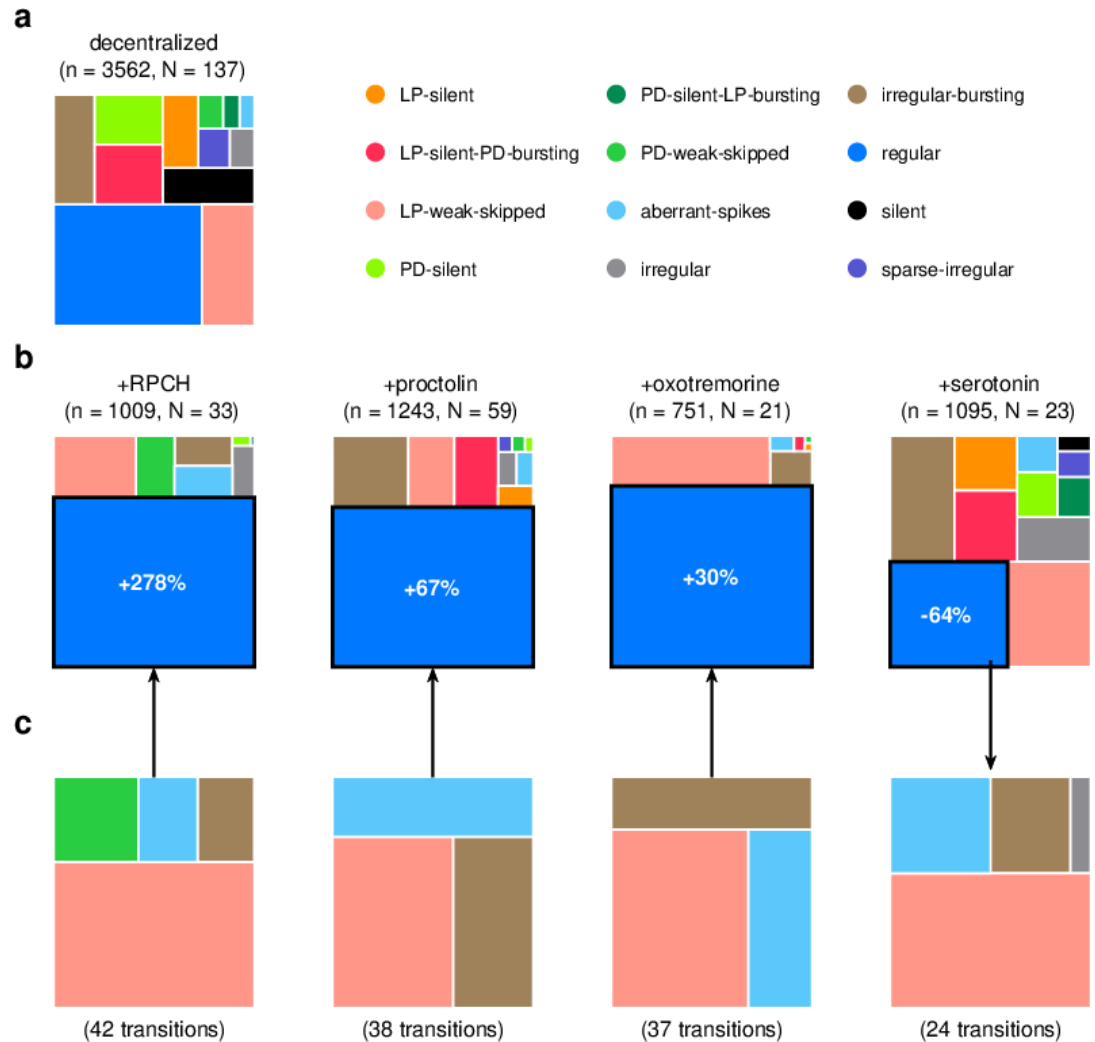


Figure 9. Effect of bath applied modulators. (a) State distribution in decentralized preparations. (b) State distribution on bath application of neuromodulators. Change percentages show difference in probability of regular state from decentralized to addition of neuromodulator. (c) Probability distribution of states conditional on transition to (for RPCH, proctolin and oxotremorine) or from (for serotonin) the regular state. (d) Coefficient of variation (CV) of burst periods of PD (purple) and LP (red) neurons vs. time before a transition away from regular states. ρ, p from Spearman test. n is the number of data points, N is the number of animals.

Figure 9-Figure supplement 1. Raw traces during proctolin application

Figure 9-Figure supplement 2. Neuromodulators affect map occupancy

407 neuromodulators were added to decentralized preparations so that endogenous effects of these
408 (and other) neuromodulators were minimized. We therefore first characterized the distribution of
409 states in decentralized preparations where neuromodulators were subsequently added (**Figure 9a**).

410 RPCH is a neuropeptide that targets a number of cells in the circuit (**Nusbaum and Marder,**
411 **1988; Swensen and Marder, 2001**), and has been shown to increase the number of spikes per burst
412 in PD and LP, (**Dickinson et al., 2001; Thirumalai and Marder, 2002**) though it has little effect on
413 the pyloric period (**Thirumalai et al., 2006**). RPCH increased the probability of the `regular` state,
414 suggesting stabilization of the triphasic rhythm, and decreased the probability of most other atypical
415 states (**Figure 9b**, Table 3, $p < .004$, paired permutation test). Consistent with earlier studies that
416 reported that RPCH can activate rhythms in silent preparations (**Nusbaum and Marder, 1988**), the
417 probability of observing the silent state was driven to 0 in the presence of RPCH, together with
418 other atypical states such as `LP-silent` and `LP-silent-PD-bursting` (**Figure 9b**).

419 Proctolin also targets a number of cells in the circuit (**Swensen and Marder, 2001**) and strength-
420 ens the pyloric rhythm through various mechanisms: by increasing the amplitude of slow oscillations
421 in AB and LP (**Hooper and Marder, 1987; Nusbaum and Marder, 1989**), depolarizing the LP neuron
422 (**Golowasch and Marder, 1992; Turrigiano and Marder, 1993**), and increasing the number of spikes
423 per burst in LP and PD (**Hooper and Marder, 1987; Marder et al., 1986; Hooper and Marder, 1984**).
424 Oxotremorine, a muscarinic agonist, has also been shown to enhance the robustness of the pyloric
425 rhythm (**Bal et al., 1994; Haddad and Marder, 2018; Rosenbaum and Marder, 2018**). Similar to
426 RPCH, both proctolin and oxotremorine significantly increase the probability of seeing the `regular`
427 state (**Figure 9b**, Table 3, $p < .004$, paired permutation test), and the `regular` state is the only one
428 significantly more likely when the neuromodulator is added. The strengthening effects of RPCH and
429 oxotremorine are also manifested in the significantly lower probabilities of observing atypical and
430 dysfunctional states such as `silent`, `LP-silent`, `PD-silent`, and `sparse-irregular` (Table 3).

431 Serotonin can have variable effects on the pyloric circuit, varying from animal to animal, and
432 can either speed up or slow down the rhythm (**Beltz et al., 1984; Spitzer et al., 2008**). In *Panularis*,
433 serotonin depolarizes LP in culture, but hyperpolarizes LP *in situ*, unlike other neuromodulators
434 which typically have the same effect *in situ* and in culture (**Turrigiano and Marder, 1993**). Consistent
435 with earlier work in *C. borealis* showing that serotonin destabilizes the rhythm in decentralized
436 preparations (**Haddad and Marder, 2018**), we found that the probability of seeing `regular` states
437 was significantly lower on addition of serotonin (**Figure 9b**, Table 3, $p < .004$, paired permuta-
438 tion test), together with a significantly higher probability of seeing atypical dysfunctional states
439 such as `LP-silent`, `aberrant-spikes`, `PD-silent-LP-bursting` and `irregular`, suggesting loss of
440 coordination between the many neurons in the pyloric circuit with serotonin receptors (**Clark, 2004**).

441 Do these modulators share common features in how they (de)stabilize the rhythm? We com-
442 puted the probability distribution of states conditional on transitions to the `regular` state for RPCH,
443 proctolin and oxotremorine, and conditional on transitions from the `regular` state for serotonin
444 (**Figure 9c**). For all four neuromodulators, the conditional state distribution was predominantly
445 comprised of these three states: `LP-weak-skipped`, `irregular-bursting` and `aberrant-spikes`, sug-
446 gesting that trajectories of recovery or destabilization of the regular rhythm share common features.
447 Serotonin destabilizes the rhythm, decreasing the likelihood of observing `regular` states, similar to
448 environmental perturbations (**Figure 5**) and decentralization (**Figure 7**).

449 Different neuromodulators activate different forms of the rhythm (**Marder and Weimann, 1992;**
450 **Marder and Hooper, 1985; Marder, 2012**), partly because different neuron types express different
451 receptors to varying extents (**Garcia et al., 2015**). Moreover, similar rhythmic motor patterns
452 can be produced by qualitatively different mechanisms, such as one that depends on voltage
453 gated sodium channel activity, and one that can persist in their absence (**Harris-Warrick and**
454 **Flamm, 1987; Epstein and Marder, 1990; Rosenbaum and Marder, 2018**). To determine if different
455 neuromodulators elicit `regular` rhythms that occupy different parts of the map, we plotted the
456 location of data elicited by various neuromodulators in the full map (**Figure 9–Figure Supplement 2**).
457 `regular` data elicited by different neuromodulators tended to lie in clusters, whose distribution in

458 the map was significantly different between serotonin and CCAP, and proctolin and every other
 459 neuromodulator tested ($p < .05$, two-dimensional Kolmogorov Smirnov test, using the method
 460 of *Peacock (1983)*). The differential clustering of regular states in the map with neuromodulator
 461 suggests that neuromodulators can elicit characteristic, distinct rhythms.

Table 3. Probability distribution of states during modulator application, as shown in *Figure 9*

State	Decentralized	RPCH	proctolin	oxotremorine	serotonin
regular	0.39	0.73	0.69	0.78	0.27
LP-silent	0.06	0	0.02	0	0.07
LP-silent-PD-bursting	0.09	0	0.07	0	0.1
PD-silent	0.07	0	0	0	0.04
PD-silent-LP-bursting	0.01	0	0	0	0.03
aberrant-spikes	0.01	0.04	0.01	0.01	0.03
LP-weak-skipped	0.14	0.11	0.07	0.17	0.19
PD-weak-skipped	0.02	0.05	0	0	0
sparse-irregular	0.03	0	0.01	0	0.02
irregular	0.02	0.02	0.01	0	0.07
silent	0.07	0	0	0	0.01
irregular-bursting	0.1	0.04	0.11	0.03	0.17

462 Neuromodulators differentially affect transition between states

463 RPCH, proctolin and oxotremorine activate a common voltage dependent modulatory current, I_{MI}
 464 (*Swensen and Marder, 2001*), but can differentially affect neurons in the STG because different cell
 465 types express receptors to these modulators to different degrees. For example, RPCH activates I_{MI}
 466 strongly in LP neurons, but the effects of oxotremorine and proctolin are more broadly observed
 467 in the circuit (*Swensen and Marder, 2000, 2001*). Though these three modulators strengthen the
 468 rhythm, only rhythms elicited by oxotremorine and RPCH persist in tetrodotoxin, and proctolin
 469 rhythms do not, hinting that qualitatively different mechanisms underlie the generation of these
 470 seemingly similar rhythms (*Rosenbaum and Marder, 2018*). We therefore measured the transition
 471 rates between states during neuromodulator application to how similar or different trajectories
 472 towards recovery were.

473 In RPCH, proctolin and oxotremorine application, ≈ 100 transitions were observed between
 474 states (*Figure 10*). Transitions could not always be predicted by a null model assuming that transi-
 475 tion probabilities scaled with the conditional probability of observing states after a transition. For
 476 example, some transitions, such as the transition from irregular to regular were never observed
 477 in RPCH, a significant deviation from the expected number of transitions given the likelihood of
 478 observing regular states after transitions (Methods and Materials). Others, such as the transi-
 479 tion LP-silent to LP-silent-PD-bursting in proctolin and oxotremorine, were observed at rates
 480 significantly higher than expected from the null model. Strikingly, no transition is significantly
 481 over- or under-represented except the transitions from regular to irregular-bursting and to
 482 LP-weak-skipped across all three stabilizing modulators. Transitions into regular state are dis-
 483 tributed across aberrant-spikes, LP-weak-skipped and irregular-bursting states for all three,
 484 but no invariant feature emerges in the rest of the transition matrix.

485 Serotonin destabilizes the rhythm in decentralized preparations, and the transition matrix under
 486 serotonin reveals several features of the irregularity behavior observed under serotonin (*Figure 10*).
 487 A number of irregular and low-firing states states from silent to irregular never transition into
 488 the regular state, which is unlikely in the null model ($p < .05$, Methods and Materials). Transi-
 489 tions between pairs of states are symmetric and occur at rates significantly larger than in the null

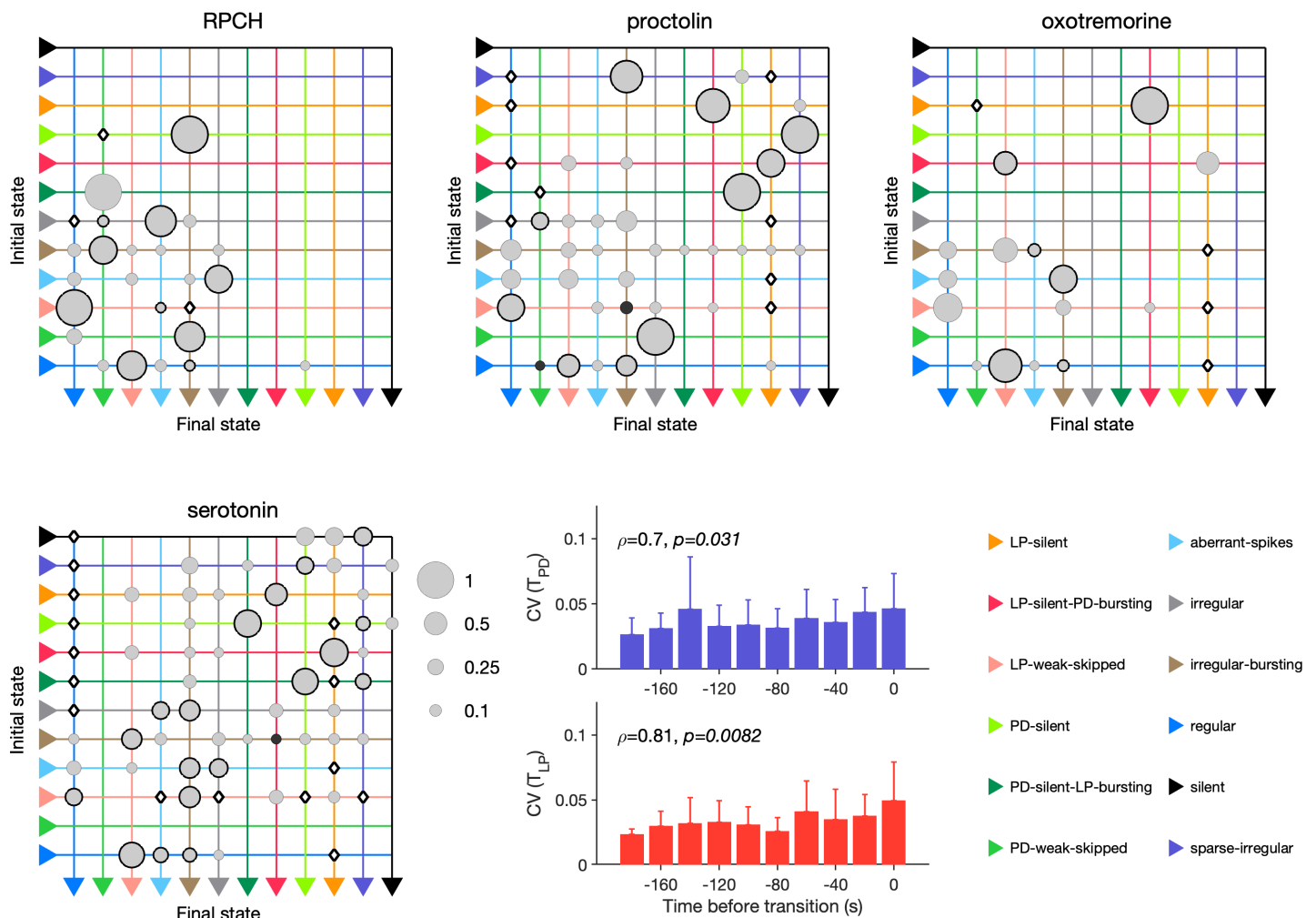


Figure 10. Effect of RPCH, proctolin, oxotremorine and serotonin on transition probabilities. Each matrix shows the conditional probability of observing the final state in the next time step given an observation of the initial state during bath application of that neuromodulator. Probabilities in each row sum to 1. Size of disc scales with probability. Discs with dark borders are transitions that are significantly more likely than the null model (Methods and Materials). Dark solid discs are transitions with non-zero probability that are significantly less likely than in the null model. \diamond are transitions that are never observed, and are significantly less likely than in the null model. States are ordered from *regular* to *silent*. Bar graphs show the coefficient of variability (CV) of PD and LP burst periods before transition away from *regular* states during serotonin application. ρ, p from Spearman rank correlation test. RPCH: $n = 148$ transitions in $N = 33$ animals. Proctolin: $n = 155$ transitions in $N = 59$ animals. Oxotremorine: $n = 102$ transitions in $N = 21$ animals. Serotonin: $n = 263$ transitions in $N = 23$ animals. Bar graphs show the coefficient of variability (CV) of burst periods of PD and LP vs time before a transition away from *regular* states during serotonin application. ρ, p from Spearman rank correlation test.

490 model, such as between LP-silent and LP-silent-PD-bursting. Intriguingly, destabilizing transi-
 491 tions from *regular* to LP-weak-skipped, aberrant-spikes and irregular-bursting are observed
 492 at rates significantly higher than in the null model. These three abnormal states are also observed
 493 immediately preceding *regular* states in RPCH, proctolin and oxotremorine (Figure 9c), suggest-
 494 ing that mechanisms for both stabilization and destabilization of the rhythm share stereotyped
 495 trajectories.

496 Are transitions away from *regular* states also associated with increases in variability of burst
 497 periods? Similar to preparations in high $[K^+]$ and low pH, and when decentralized, transitions away
 498 from *regular* states in serotonin were associated with significantly rising variability in the burst
 499 periods of PD and LP neurons (Figure 10, $p < .05$, Spearman rank correlation test).

500 Discussion

501 This study provides a concrete example of why it can be difficult to characterize experimental
502 observations without the appropriate vocabulary to do so. Both highly stereotyped rhythms such
503 as the pyloric oscillation, and highly irregular Poisson-like firing in large brain circuits are routinely
504 described quantitatively using summary statistics. In the intermediate region between order and
505 disorder, dynamics are harder to describe, and therefore frustrate efforts to systematically study
506 circuits that generate them. We show that an unsupervised dimensionality reduction algorithm like
507 t-SNE can create a useful representation of a dataset that is too large to visualize in its entirety using
508 traditional methods. We incorporated domain-specific expert knowledge into this unsupervised
509 approach by manually segmenting and labelling clusters in the embedding, identifying clusters of
510 dynamics with biologically significant behavior. This dual approach conferred a two-fold advantage:
511 both to more accurately measure traditional metrics such as burst metrics in regular states in large
512 datasets (**Figure 4**, **Figure 8**), and to analyze irregular dynamics beyond the remit of conventional
513 analysis methods (e.g., **Figure 9**). The map created in the present study (**Figure 2**) can be used as a
514 blueprint to contextualize new experimental data from future experiments, which in turn can be
515 added to the map to create a more complete picture of pyloric circuit dynamics.

516 Robust identification of regular rhythms allows for detailed, interpretable analysis 517 of rhythm metrics

518 Measuring the mean and variability of a regular oscillation in a neural circuit has several subtle
519 challenges. Typically, variations in estimated metrics arising from cycle-to-cycle fluctuations are not
520 distinguished from those arising from alteration between regions of regular bursting interrupted by
521 regions of irregular spiking where these metrics are not defined. One way to disambiguate the two
522 is to construct elaborate checks to make sure that the spike pattern being measured meets certain
523 criteria. However, edge cases abound, and this is a challenging and poorly-motivated approach. One
524 consequence of the embedding method we used is to reliably identify when rhythms were regular,
525 and we found that burst metrics were well defined for this subset of data. We were therefore able
526 to measure the mean and variability of various burst metrics (**Figure 4**), confident that we were
527 measuring these metrics only in stretches of data where it made sense to do so. A byproduct of
528 this restriction is that the variability in burst metrics measured this way stems almost entirely from
529 cycle-to-cycle variations.

530 Consistent with years of study (*Bucher et al., 2005; Hamood and Marder, 2015; Hamood et al.,*
531 **2015**), our results (**Figure 4**) show explicitly that within-animal variability in pyloric burst metrics
532 is less than across-animal variability. Our results are from a meta-analysis of data from several
533 different experimenters from different laboratories, collected over a span of ten years. It is therefore
534 an ideal dataset in which to measure variability. We find that the coefficient of variation of all burst
535 metrics measured is ≈ 0.1 (**Figure 4b**), which is a proxy for how regular the pyloric oscillation can
536 be under baseline conditions. Measuring burst metrics on decentralization (**Figure 8**) also allowed
537 us to characterize how regular rhythms change, while still being recognizably regular. In addition
538 to recapitulating well-understood phenomena such as the slowing down and increased variability
539 in rhythms, we found that phase of LP burst starts did not significantly change, but phases of LP
540 bursts stops did, suggesting that features of the rhythm are differentially robust to the removal of
541 neuromodulation.

542 Numerical methods to analyze neural circuit dynamics

543 Advances in experimental techniques in neuroscience allow for recordings from larger number
544 of neurons for longer periods. There have been contemporaneous advances in techniques to
545 analyze this data. A first step in data analysis is often data visualization. Modern neural data can
546 be large and high dimensional, and visualizing the entirety of a large data set can be a non-trivial
547 task. Visualization and other forms of data analysis rely on dimensionality reduction (*Nguyen and*
548 **Holmes, 2019**).

549 Here we used the t-SNE algorithm as a core method to reduce the dimensionality of the dataset
550 and to visualize our data. t-SNE has been widely used in the unsupervised analysis of many types
551 of biological data (*Berman et al., 2014; Kollmorgen et al., 2020; Chen et al., 2020; Macosko et al.,*
552 *2015; Kobak and Berens, 2019; Leelatian et al., 2020*), including neural recordings (*Dimitriadis*
553 *et al., 2018*). t-SNE minimizes the Kullback-Leibler divergence between a Gaussian distribution
554 modeling pairwise distances between data points and a Student t-distribution modeling distances
555 between the same points in a low (typically two) dimensional embedding (*Van der Maaten and*
556 *Hinton, 2008; Linderman and Steinerberger, 2019*). This feature makes t-SNE an attractive tool to
557 try to visualize data sets such as the data in this paper, because it can demonstrate how similar
558 spike patterns are to each other.

559 t-SNE has also been used to find clusters in data, since its original use in visualizing and
560 clustering hand-written digits in the MNIST database (*Van der Maaten and Hinton, 2008*). t-SNE
561 has been shown rigorously to be capable of recovering well-separated clusters (*Linderman and*
562 *Steinerberger, 2019*). Neighborhood embedding techniques like t-SNE combine attractive forces
563 between pairs of points with repulsive forces between all points. Stronger attraction can better
564 represent smoothly varying manifold structures, while stronger repulsion can better represent
565 discrete cluster structures (*Böhm et al., 2020*). In our application, t-SNE generated clusters where
566 spike patterns could be described as qualitatively different. For example, spike patterns in top-most
567 cluster (colored green in *Figure 3*) all had weak PD spiking, but regular and strong LP spiking. This
568 was qualitatively different from the two closest clusters LP-weak-skipped and irregular. In regions
569 of the map where clusters were not cleanly separated (for example, in the connection between the
570 regular and irregular-bursting clusters), manual inspection revealed a number of intermediate
571 states. The "clustered" or "not-clustered" regions of the map are therefore informative of the
572 underlying distribution of spike patterns, and emerge robustly from the embedding.

573 t-SNE-based methods are not the only way to analyze such data, and a variety of other methods
574 have been developed recently. Multidimensional Scaling (MDS) (*Cox and Cox, 2008*) has been
575 used to visualize collective coding for different task dimensions in a population of neurons in the
576 amygdala in rats (*Kyriazi et al., 2018*). Convolutional non-negative matrix factorization (*Mackevicius*
577 *et al., 2019*) has been used to find sequences in neural and behavioral data by building a parts-
578 based representation of the data. Recent work (*Williams et al., 2020*) extends this method by
579 including a point process model to model sparse spike sequences without binning time. Tensor
580 Component Analysis (*Williams et al., 2018*) can generate three low-dimensional descriptions from
581 neural data: separating out neuron-specific, trial-specific and temporal factors, making it valuable in
582 multi-trial data. Dynamical Component Analysis is a linear method that attempts to find dynamics
583 rather than explaining variance in the data (as in PCA) (*Clark et al., 2019*).

584 Methods based on neural networks offer powerful tools to analyze unstructured neural data.
585 Generally, one method to study how a high-dimensional neural system works is to model it with a
586 recurrent neural net (RNN), and then to study the RNN model (*Vyas et al., 2020*). Autoencoders offer
587 an interesting way of dimensionality reduction (or latent space analysis) because their architecture
588 contains an information bottleneck (*Rumelhart et al., 1985*), and have long been a focus of unsu-
589 pervised machine learning (*Baldi, 2012*). Topological autoencoders combine autoencoders with the
590 concept of persistent homology, and use a topological loss term that minimizes differences between
591 the topological signatures of the data and the representation in the lower dimensional space (*Moor*
592 *et al., 2019*). These methods are similar in spirit to the analysis presented here, but use sophisti-
593 cated neural nets whose parameters yield the lower-dimensional representation. Other end-to-end
594 analysis methods include a method called SOM-VAE, which combine self-organizing maps (SOMs)
595 and variational auto-encoders (VAEs) (*Fortuin et al., 2018*) to analyze high dimensional time series
596 and find transitions between states, and deep temporal clustering, which combines dimensionality
597 reduction and temporal clustering in a single unsupervised learning problem (*Madiraju et al., 2018*).

598 **Applicability to bigger circuits and unidentified neurons**

599 In this study, we used spiking patterns of PD and LP cells as a proxy for the dynamics of the
600 pyloric circuit. A better characterization of pyloric circuit dynamics would include AB, PY, VD and IC
601 cells (*Eisen and Marder, 1982; Marder and Bucher, 2007*). The data analyzed in this study did not
602 consistently have recordings that made it possible to reliably and consistently extract spike times of
603 the VD and PY neurons. While most of the data included recordings from the *lvn* nerve, extracting
604 PY spike times from the *lvn* was not feasible at scale. Spikes from PY are smaller than spikes from LP
605 and PD on the *lvn*, and the duration of PY bursting may partially overlap with that of LP and PD. Even
606 when data include recordings from the *pyn*, identifying PY spikes is not straightforward. There are
607 several PY neurons, whose spikes may overlap to varying degrees to variability in the subpopulation
608 of PY neurons that spike and the precise timing of action potential initiation. The shape of PY spikes
609 can therefore be quite variable. In addition, spikes from the gastro-pyloric LPG neuron are often
610 observed on the *pyn* (*Figure 1b*). Even intracellular recordings from PY neurons are not necessarily
611 sufficient to accurately estimate PY spike times because intracellular recordings measure the activity
612 of only the cell recorded from, and it is not uncommon to observe that the PY cell being recorded
613 from generates fewer spikes than the other PY neurons as observed extracellularly, possibly due to
614 leak currents introduced from sharp electrodes (*Cymbalyuk et al., 2002*).

615 In this analysis, we chose to include features such as the "spike phase" (*Figure 2b-c*) because the
616 neurons in this circuit are mutually coupled with inhibitory and electrical synapses and therefore
617 strongly affect the activities of each other in the collective rhythm. An analysis of circuit dynamics
618 from other neural networks that did not show such strong intrinsically phase-controlled behavior
619 could use other features more suitable to those systems. The analysis method in this study is
620 well-suited for large datasets of neural recordings from identified neurons. Data where the identity
621 of each neuron is not uncontrolled, or cannot be known, such as large scale recordings from a brain,
622 would require modifications to the analysis pipeline described in *Figure 2*. First, it would no longer
623 be possible to construct a data vector of fixed length, because ordering of the different neurons
624 would not be meaningful. Each data point would instead be an unordered set of spike times from
625 each neuron, and a distance function that operated on spike times (*Christen et al., 2006; Victor and*
626 *Purpura, 1997; Schreiber et al., 2003; Rossum, 2001*) could be used to generate a distance matrix
627 between raw data points, which would be the input to the embedding algorithm.

628 **Ahead-of-time experimental design can maximize utility and interpretability of** 629 **data**

630 This study used a large dataset collected by various experimenters, and included data originally
631 collected for other studies (*Tang et al., 2012, 2010; Haddad and Marder, 2018; Haley et al., 2018;*
632 *Rosenbaum and Marder, 2018; Powell et al., 2021; He et al., 2020*). As such, this post-hoc analysis
633 is limited ultimately by the data: its quantity, the way it was collected, and the decisions made
634 and tradeoffs chosen by the experimenter who collected it. A general lesson learned here is that
635 close coordination between experimenters and theorists and data analysts can help maximize the
636 utility of data collected. Because experiments are expensive to perform, in the time of researchers,
637 reagents and experimental animals, seemingly inconsequential changes to the way data are col-
638 lected can substantially increase the amount of usable data to a greater number of questions, some
639 of which may not be well-formulated at the time of data collection.

640 For example, studying the effects of perturbations to pyloric circuits forces experimenters to
641 make choices about experimental protocol that have far-reaching consequences on the analysis and
642 interpretation of data collected. If perturbations are severe enough to destabilize the pyloric rhythm,
643 and even cause prolonged periods of silence, should an identical sequence of perturbations be
644 used in every preparation if some preparations "crash" under relatively moderate perturbations and
645 greater perturbations may risk irreversible changes? Is it more important to introduce perturbations
646 that change at a certain, fixed rate, or should perturbation intensity be dialed up or down based on
647 observed responses, to better characterize the full response range of the system being perturbed?

648 Experimental constraints and the priorities of specific studies have led to a patchwork of choices in
649 the dataset used here, which means that it is not entirely straightforward to disentangle the effects
650 of applied perturbations at a given time from the cumulative effects of the entire experimental
651 protocol and stimulus history.

652 Data acquisition systems allow experimenters to record from neurons at high temporal res-
653 olution for long periods of time. Time-varying metadata, such as pH, temperature, $[K^+]$ or the
654 concentration of added modulators are not always recorded concomitantly, because they can
655 be difficult to measure. Temperature and pH probes, when used, can yield high-resolution and
656 automatic logging of these quantities. Because decentralization involves a manual intervention
657 such as cutting the *stn* or constructing and filling a well on the *stn*, and because the process takes
658 time, the precise time of decentralization can be hard to record and estimate, leading to a fraction
659 of preparations being decentralized before the nominal start of decentralization, with effects being
660 evident as in the apparent increase in burst period shown in *Figure 8d*.

661 **Cryptic circuit variability can be revealed by diversity in crashes**

662 A large body of work has shown that there is more than one way to make a functional neural circuit
663 (*Prinz et al., 2003, 2004; Gutierrez et al., 2013*). Several combinations of circuit parameters such as
664 synapse strengths, ion channel conductances and network topology can be found in circuits that
665 generate similar emergent collective dynamics (*Gonçalves et al., 2020*). In the pyloric circuit, the
666 dimensionality of the space of neuron and circuit parameters is larger than the dimensionality of the
667 rhythm: ≈ 50 parameters are required to specify ionic and synaptic conductances even in simplified
668 models, but the rhythm under baseline conditions can be well described using a handful of metrics
669 (*Marder and Bucher, 2007*). This disparity in dimensionality leads to an inherently many-to-one
670 mapping from the space of circuit architecture to the space of circuit dynamics. Pyloric circuits at
671 baseline can therefore exhibit "cryptic" architectural variability (*Haddad and Marder, 2018*), where
672 the diversity of circuit topologies and neuron parameters underlying functional circuits is masked
673 by the relatively low-dimensional nature of the observation of regular rhythms. Intriguingly, there
674 was no seasonal effect on the variations in bursting under baseline conditions (*Figure 4–Figure*
675 *Supplement 4*), or sensitivity to decentralization (*Figure 7–Figure Supplement 4*), suggesting that
676 these dimensions of observed variability may arise from other factors such as circuit-to-circuit
677 architectural differences.

678 Perturbations can reveal differences between seemingly identical circuits because parameter
679 differences that were inconsequential in the generation of baseline activity can now generate
680 disparate dynamics. Perturbations such as current injections in a network of oscillators can shift
681 phases, revealing connection weights between individual neurons (*Timme, 2007*). What do the
682 perturbations used in this work do? Some perturbations like decentralization can have complex,
683 time varying and variable effects, because neurons in the STG are multiply modulated (*Marder,*
684 *2012*); this may lead to the complex and diverse responses seen on decentralization (*Figure 7*).
685 Others like changing extracellular $[K^+]$ can have more focussed effects, which changes the reversal
686 potential of K^+ ions, altering currents through K^+ permeable ion channels, and tends to depolarize
687 neurons (*He et al., 2020*). The challenge in interpreting data from experiments with perturbations
688 such as these is the dual complexity of the elicited circuit behavior and the functional effects of the
689 perturbations. Future work with other, sparse perturbations can help determine if diverse dynamics
690 observed in the present work are a consequence of the complex nature of the perturbations used.

691 If there are many solutions to a designing a functional circuit, are some solutions more robust to
692 all perturbations? Alternatively, is there a tradeoff for circuits between being robust to perturbation
693 X and being robust to perturbation Y ? At the population level, some animals could possess pyloric
694 circuits more robust to one perturbation, and the expense of greater sensitivity to another; and
695 other animals could possess circuits that are more robust to other perturbations. Recent work
696 studying a population of isolated pacemaker kernels of the pyloric circuit (AB and PD cells) found
697 only moderate correlation between robustness to perturbations in pH and temperature (*Ratliff*

698 *et al., 2021*). Examples of population-level hedges against uncertain environmental perturbations
699 include the diversity in chemotactic behavior in bacteria (*Frankel et al., 2014*). In modeling work with
700 neurons, recent work has shown that homeostatic regulation rules that confer robustness to some
701 perturbations can create sensitivity to other perturbations (*O'Leary et al., 2014; Gorur-Shandilya*
702 *et al., 2020*).

703 **Linking behavior to mechanisms**

704 The present work offers a path towards analysis that can reveal cryptic variability and build mecha-
705 nistic links from circuit architecture to function. By characterizing the totality of circuit dynamics
706 under a variety of conditions, this study equips further work with the tools to fit biophysically
707 detailed models of the pyloric circuit to diverse circuit dynamics under baseline conditions and
708 perturbations. From the large diversity of neuron and circuit parameters that can reproduce a
709 snapshot of activity, will only a subset of models recapitulate the diverse irregular behavior seen
710 under extreme perturbations? Recent work that reproduced how circuits change cycle periods
711 with temperature (*Alonso and Marder, 2020*) can be extended to find parameter sets that also
712 generate the irregular states characterized in this study, at the rates observed in the data, and will
713 help resolve this question. Future experimental work can pair data analysis methods such as this
714 work with quantitative measurements of cellular and circuit parameters using emerging techniques
715 (*Schulz et al., 2006, 2007; Tobin et al., 2009*) to find parameter values of cells that generate robust
716 rhythms and irregular states.

717 **Diversity and stereotypy in trajectories from functional to crash states**

718 Are there preferred paths to go from regular rhythms to crash? Diversity in the solution space of
719 functional circuits, and the varied effects of perturbations on these circuits, argue for an assortment
720 of trajectories from function dynamics to irregular or silent states. While transition matrices
721 measured during different perturbations were varied (*Figure 6*), we did observe universal features
722 in transition matrices measured during environmental perturbations, decentralization, and addition
723 of neuromodulators (*Figure 6, Figure 7, Figure 10*). The destabilizing transition from `regular` →
724 `LP-weak-skipped` was over-represented in every transition matrix, suggesting that the weakening
725 of the LP neuron is a crucial step in the trajectories towards destabilization, perhaps because there
726 is only one copy of LP in the circuit. Earlier work studying trajectories of destabilization of regular
727 bursting in the isolated pacemaker kernel also found a common trajectory of destabilization, from
728 regular bursting to tonic spiking to silence (*Ratliff et al., 2021*). Transitions away from `regular`
729 rhythms were also associated with increased variability in burst periods during all perturbations
730 except high temperature and low pH (*Figure 6, Figure 7, Figure 10*). Earlier work on the isolated
731 pacemaker kernel found similar increase in variability in PD voltage dynamics before transitions
732 from regular bursting, similar to the increasing variability measured in the present study (*Ratliff*
733 *et al., 2021*).

734 The structure of the transitions between states also hints at features of the circuit that are critical
735 for rhythm (de)stabilization. Unsurprisingly, `PD-silent` states precede `silent` states in low pH, high
736 temperature and high $[K^+]$ perturbations (*Figure 6*). This makes sense because PD cells are electri-
737 cally coupled to the endogenous burster AB in the pacemaker kernel, and silencing the pacemaker
738 kernel can cause the circuit to go silent. Though the states are determined purely from clusters
739 in the embedding (*Figure 2*), and thus from statistical features of spike times, some states may be
740 identified predominantly with cell-specific features (e.g., `LP-weak-skipped` where the LP neuron
741 fails to burst regularly, but the PD neurons do), or with circuit-level features (e.g., `aberrant-spikes`
742 where one or both neurons fire spikes outside the main burst, which may be caused by incomplete
743 inhibition from the reciprocal neuron). Decentralization elicits the largest number of transition
744 types, with $\approx 80\%$ of all transition types observed, which could be a consequence of the complex
745 change in the neuromodulator milieu following transection of descending nerves.

746 **Comparison with other categorization methods**

747 Earlier work categorized the varied dynamics of the pyloric circuit during perturbations (*Haddad*
748 *and Marder, 2018; Haley et al., 2018; Ratliff et al., 2021; Alonso and Marder, 2020*). In that work,
749 categories were typically constructed by hand and were not rigorously shown to be mutually exclu-
750 sive. Categories in the present work, while being manually chosen, emerge from the distribution of
751 the data in the map (*Figure 3*); and no segment of data can have more than one label, because it can
752 exist only at a single point in the map. Earlier work categorized rhythms that were labelled *regular*
753 into two categories, "normal triphasic" and "normal triphasic slow" (*Haddad and Marder, 2018*).
754 While there is significant variation in the burst periods in the *regular* cluster, (*Figure 2–Figure*
755 *Supplement 1, Figure 4*), we did not observe a distinctly bimodal distribution of burst periods,
756 and therefore could not justify splitting *regular* into two. Earlier work also included a category
757 called "gastric like rhythms", where LG or DG neurons were active, indicating the presence of the
758 gastric mill (*Weimann and Marder, 1994*). Because the present work only considers spikes on PD
759 or LP neurons, circuit dynamics with gastric activity are scattered across states, based on how the
760 gastric activity affects PD and LP spikes. The "LP01" state identified in *Haddad and Marder (2018)*
761 is equivalent to the LP-weak-skipped state; the present work also identified a PD-weak-skipped
762 which was not identified in the earlier work, perhaps because it is $\approx 1/7$ as prevalent (*Figure 3*). The
763 catch-all "atypical firing" state could be teased apart into a number of irregular states (*irregular,*
764 *irregular-bursting, sparse-irregular*) that span several well-separated clusters in the map (*Fig-*
765 *ure 3*). In summary, the present work recapitulates every label constructed to categorize spike
766 patterns from PD and LP neurons in earlier work, and additionally finds new spike patterns that
767 were either not detected or not identified as distinct.

768 Our work provides a key tool to characterize non-regular spike patterns in small neural circuits
769 and thus provides a bridge between experimental or simulation work grounded in the biophysical
770 detail of ion channels and synaptic currents; and the rich body of observations of circuits under
771 baseline and challenging conditions. The tools we have employed can easily be adapted to other
772 circuits and systems, makes limited assumptions of the dynamics of the circuit, yet provides a robust
773 framework on which to hang a large volume of previously ineffable expert domain knowledge.

774 **Methods and Materials**

775 **Animals and experimental methods**

776 Adult male Jonah crabs (*C. borealis*) were obtained from Commercial Lobster (Boston, MA), Seabra's
777 Market (Newark, NJ) and Garden Farm Market (Newark, NJ). Dissections were carried out as previ-
778 ously described (*Gutierrez and Grashow, 2009*). Decentralization was carried out either by cutting
779 the *stn*, or by additionally constructing a well on the *stn* and adding sucrose and TTX as described in
780 *Haddad and Marder (2018)*. Temperature was controlled as described in *Tang et al. (2012, 2010);*
781 *Haddad and Marder (2018)*. Extracellular potassium concentrations were varied as described in *He*
782 *et al. (2020)*. pH perturbations are described in *Haley et al. (2018)*.

783 **Spike identification and sorting**

784 Spikes are identified from extracellular recordings of motor nerves or from intracellular recordings.
785 LP spikes were identified from intracellular recordings, *lvn*, *lpn* and *gpn* nerves (in descending order
786 of likelihood). PD spikes were identified from *pdn*, intracellular recordings, and *lvn*. We used a
787 custom-designed spike identification and sorting software (called "crabsort") that we have made
788 freely available at <https://github.com/sg-s/crabsort> previously described in *Powell et al. (2021)*.
789 Spikes are identified using a fully connected neural network that learns spike shapes from small
790 labelled data sets. A new network is typically initialized for every preparation. Predictions from
791 the neural network also indicate the confidence of the network in these predictions, and uncertain
792 predictions are inspected and labelled and the neural network learns from these using an active
793 learning framework (*Settles, 2009*).

794 **Data curation and data model**

795 Each file was split into 20-second non-overlapping bins and spike times, together with metadata,
796 were assembled into a single immutable instance of a custom-built class (`embedding.DataStore`).
797 The data store had the following attributes:

- 798 • *spike times* containing LP and PD spike times.
- 799 • *ISIs* containing inter-spike intervals and spike phases
- 800 • *labels* categorical data containing manually generated labels from **Figure 3**
- 801 • *metadata* such as concentration of modulators, pH, temperature, whether the preparation
802 was decentralized or not, etc.

803 Using an immutable data structure reduced risks of accidental data alteration during analysis.
804 Every attribute was defined for every data point.

805 **Embedding**

806 ISI and phase representation (**Figure 2b**)

807 Each data point is a 20-second bin containing spike times from LP and PD neurons (**Figure 2a**). For
808 each data point, spike times are converted into inter-spike intervals. A set of spike times uniquely
809 identifies a set of (ordered) inter-spike intervals. The set of LP spike times generates a set of LP ISIs,
810 and the set of PD spike times generates a set of PD ISIs (**Figure 2b**).

811 For every spike in PD or LP, a "spike phase" can be calculated as follows. Spike phases are not
812 defined when either LP or PD are silent in that data point, or for LP/PD spikes with no spikes from
813 the other neuron before or after that spike. Thus the "spike phase" of the i -th spike on neuron X
814 w.r.t neuron Y is given by:

$$\frac{t_i^X - t_{i,-}^Y}{t_{i,+}^Y - t_{i,-}^Y} \in [0, 1]$$

815 where t_i^X is the time of the i -th spike on neuron X, $t_{i,-}^Y$ is the time of the last spike on Y before
816 t_i^X and $t_{i,+}^Y$ is the time of the first spike after t_i^X . Note that this definition can be generalized to N
817 neurons, though the number of spike phases grows combinatorially with N .

818 Construction of vectorized data frame (**Figure 2c-d**)

819 Each data point can contain an arbitrary number of spikes, and thus an arbitrary number of ISIs
820 and spike phases. Ideally, each data point is a data frame of fixed length (a point in some fixed
821 high-dimensional space). To do so, we computed percentiles ISIs and spike phases (**Figure 2c**). We
822 chose ten bins per ISI type (deciles). The end result is not strongly dependent on the number of bins
823 chosen, as long as there are sufficiently many bins to capture the distinctly bimodal distribution in
824 ISIs during bursting.

825 We included three other features to help separate spike patterns that appeared qualitatively
826 different. First, firing rates of LP and PD neurons. Second, the ratios of 2nd-order to 1st-order ISIs,
827 defined as:

$$\frac{\max I^{(2)}}{\max I^{(1)}}$$

828 where $I^{(n)}$ is the n -th order set of ISIs computed as time the time between n spikes. $I^{(1)}$ is the
829 simple set of ISIs defined between subsequent spikes. This measure is included because it captures
830 the difference between single spike bursts and normal bursts well.

831 Finally, we also included a metric defined as follows:

$$\frac{\max \text{diff}(\mathbf{s})}{s_{\max}}$$

832 where \mathbf{s} is a vector of sorted ISIs and s_{\max} is the sorted ISI for which the difference between it and
833 the previous sorted ISI is maximum. This metric was included as it captures to a first approximation

834 how "burst-like" a spike train is. Intuitively, this metric is high for spike trains with bimodal ISI
835 distributions, as is the case during bursts.

836 All these features were combined into a single data frame and z-scored (**Figure 2d**).

837 In some cases, these features were not defined, e.g.: when there are no spikes on either neuron,
838 the concepts of spike phases or ISIs are meaningless. In these cases, "filler" values were used that
839 were located well off the extremes of the distribution of the metric when defined. For example, ISIs
840 were filled with values of 20s (the size of the bin) when no spikes were observed. The overall results
841 and shape of the embedding did not depend sensitively on the value of the filler values used.

842 Embedding using t-SNE

843 So far, we have described how we converted a 20-second snippet containing spike times from LP
844 and PD into a data frame (a vector). We did this for every 20-second snippet in the dataset. Data
845 that did not fit into any bin was discarded (for example, data at the trailing end of an experiment
846 shorter than 20 seconds). Thus, our entire dataset is represented by $M \times N$ matrix where M is the
847 number of features in the data frame and N is the number of data points.

848 We used the t-SNE algorithm (**Van der Maaten and Hinton, 2008**) to visualize the vectorized data
849 matrix in two dimensions. Our dataset contained $\approx 10^5$ points, and was therefore too large for
850 easy use of the original t-SNE algorithm. We used the FI-tSNE approximate algorithm (**Linderman
851 et al., 2019**) to generate these embeddings. We used a perplexity of $P = 100$ to generate these
852 embeddings. Varying perplexity caused the embedding to change in ways consistent with what
853 is expected for t-SNE embeddings, and the coarse features of the embedding did not sensitively
854 depend on this choice of perplexity (**Figure 2–Figure Supplement 3**).

855 t-SNE is often used with random initialization, and different random initializations can lead
856 to different embeddings with clusters located at different positions in the map. The importance
857 of meaningful initializations has recently been highlighted (**Kobak and Linderman, 2021**), and we
858 used a fixed initialization where the X-axis corresponded to the shortest ISI in each data point,
859 and the Y-axis corresponded to the maximum ratio of 2nd-order to 1st order ISI ratios (described
860 above). For completeness, we also generated embeddings using other initializations (**Figure 3–
861 Figure Supplement 2**). For both random initializations (**Figure 3–Figure Supplement 2a-d**) and
862 initializations based on ISIs (**Figure 3–Figure Supplement 2e-f**), we observed that regular states
863 tended to occur in a single region, surrounded by clusters that were dominated by a single color
864 corresponding to irregular states. Thus, the precise location of different clusters can vary with the
865 initialization, but the overall structure of the embedding, and the identity of points that tend to
866 co-occur in a cluster, does not vary substantially with initialization.

867 Triangulation and triadic differences (**Figure 2–Figure Supplement 2**)

868 The output of the embedding algorithm is a set of points in two dimensions. We built a Delaunay
869 triangulation on these points. For each triangle in the triangulation, we computed the maximum
870 difference between some burst metric (e.g., burst period of PD neurons) across the three vertices
871 of that triangle. These triadic differences are represented colored dots, where the dots are located
872 at the incenters of each triangle in the triangulation.

873 Time series analysis

874 Measuring transition matrices (**Figure 6, Figure 7, Figure 10**)

875 The transition matrix is a square matrix of size N that describes the probability of transitioning from
876 one to another of N possible states. The transition matrix we report is the right stochastic matrix,
877 where rows sum to 1. Each element of the matrix T_{ij} corresponds to the conditional probability that
878 we observe state j given state i . To compute this, we iterate over the the sequence of states and
879 compare the current state to the state in the next state. Breakpoints in the sequence are identified
880 by discontinuities in the timestamps of that sequence and are ignored. We then zeroed the diagonal
881 of the matrix and normalized each row by the sum.

882 Measuring variability before transitions away from regular states (**Figure 6 ,Figure 7**)
883 We first identified continuous segments that corresponded to uninterrupted recordings from the
884 same preparation at the appropriate condition. For each segment, we found all transitions away
885 from the regular state. We therefore computed a vector, as long as the segment, containing the
886 time to the next transition. We then collected points corresponding to time to next transition
887 ranging from $t = -200s$ to $t = 0s$. For each time bin, we measured the coefficient of variation of the
888 burst period by dividing the standard deviation of the burst period in that datum by the mean in
889 that datum.

890 Data visualization

891 Raincloud plots (**Figure 4**)

892 Raincloud plots (**Allen et al., 2019**) are used to visualize a univariate distribution. Individual points
893 are plotted as dots and a shaded region indicates the overall shape of the distribution. This shape
894 is obtained by estimating a kernel smoothing function estimate over the data. Individual points are
895 randomly jittered along the vertical axis for visibility.

896 Occupancy maps (**Figure 5, Figure 7**)

897 To visualize where in the map data from a certain condition occurred, the full embedding is first
898 plotted with colors corresponding to the state each point belongs to. The full dataset is made semi-
899 transparent and plotted with larger dots to emphasize the data of interest. Data in the condition
900 of interest is then plotted as usual. Each bright point in these plots corresponds to a 20-second
901 snippet of data in the condition indicated.

902 Treemaps (**Figure 7, Figure 9**)

903 Treemaps (**Shneiderman and Wattenberg, 2001**) were used to visualize state probabilities in a given
904 experimental condition. For each preparation, the probability of each state was computed, and the
905 mean probability of a given state was computed by averaging across all preparations. Thus, each
906 preparation contributes equally. The area of the region in the treemap scales with the probability of
907 that state.

908 Transition matrices (**Figure 6, Figure 7, Figure 10**)

909 Transition matrices were visualized as in **Corver et al. (2021)**. Initial states are shown along the left
910 edge and final states are shown along the bottom edge of each matrix. Lines are colored by origin
911 (horizontal lines) or destination (vertical) states. The size of each disc at the intersection of each line
912 scales with the conditional probability of moving from the initial state to the final state. Note that
913 the size of all discs is offset by a constant to make small discs visible.

914 Statistics

915 Comparing within-group to across-group variability (**Figure 4**)

916 To compare the variability of various burst metrics within each animal and across animals, we first
917 measured the means and coefficients of variations (CV) of each burst metrics in every animal. We
918 then used the mean of the coefficients of variations as a proxy for the within-animal variability, and
919 used the coefficient of variation of the means as a proxy for the across-animal variability. Note that
920 both measures are dimensionless. They can therefore be directly compared.

921 To test if the within animal variability was significantly less than the across animal variability, we
922 performed a permutation test. We shuffled the labels identifying the animal to which each data
923 point belonged to and measured a new "within-animal" and "across-animal" variability measure
924 using these shuffled labels. We repeated this process 1000 times to obtain a null distribution of
925 differences between within- and across-animal variability. Identifying where in the null distribution
926 the data occurred allowed us to estimate a p -value for the measured difference. For example, if the
927 measured difference between within- and across-animal variability in metric X was greater than

928 99% of the null distribution obtained by shuffling labels, we conclude that the p -value is .01. The
929 significance level of .05 was divided by the number of burst metrics we tested to determine if any
930 one metric was significantly more or less variable across animals.

931 Comparing map occupancy before and after decentralization (**Figure 7b**)

932 To determine if data are more widely distributed in the map after decentralization, we computed
933 the mean distances travelled in the map between subsequent time points for each preparation.
934 Each preparation's circuit dynamics is represented as a trajectory in this map. Distances in the map
935 between subsequent points are measured and summed for each preparation.

936 Each point in (**Figure 7b**) corresponds to a single preparation before and after decentralization.
937 Data are therefore paired and we can generate a null distribution by randomly shuffling each pair.
938 This null distribution is shown in the gray shading in (**Figure 7b**). The dashed line is the line of unity
939 and indicates the middle of the null distribution. The measured difference between the distances
940 travelled in the decentralized and intact cases is shown in the purple line. The p value can be
941 estimated as the fraction of the null distribution greater in magnitude than the purple line.

942 Measuring trends in variability in regular rhythms before transitions (**Figure 6b ,Figure 7f,** 943 **Figure 9d**)

944 To determine if variability significantly increased in the 200s preceding a transition away from
945 regular, we measured the Spearman rank correlation between time before transition (x-axis) and
946 mean variability. The Spearman rank correlation ρ is 1 if quantities monotonically increase.

947 Measuring transition rate significance (**Figure 6a ,Figure 7e, Figure 10**)

948 In the empirical transition matrices, certain transitions never occur, and certain transitions occur
949 with relatively high probability. Each element of the transition matrix T_{ij} corresponds to the
950 conditional probability $P(\text{final}|\text{initial})$. Our null model assumes that transitions occur at random
951 between states, and therefore the probability of observing any transition $i \rightarrow j$ scales with the
952 marginal probability of observing state j after transitions. We therefore built a null distribution of
953 transition rates by sampling with replacement from the marginal counts of states after transitions.
954 The fraction of this null distribution that was above or below the empirical transition rate was
955 interpreted to be the p -value and thus determined significance.

956 **Code availability**

957 The following table lists code used in this paper. Code can be downloaded by prefixing <https://github.com/>
958 [//github.com/](https://github.com/) to the project name.

Table 4. Code availability

project	Notes
sg-s/crabsort	interactive toolbox to sort spikes from extracellular data
sg-s/stg-embedding	Contains all scripts used to generate every figure in this paper
KlugerLab/Flt-SNE	Fast interpolation based t-SNE, used to make embedding
sg-s/SeaSurfaceTemperature	wrapper to scrape NOAA databases

959 **Acknowledgments**

960 This paper includes data collected by Lamont Tang, Lily He, Mara Rue, Jessica Haley, Daniel Powell,
961 Anatoly Rinberg, and Ekaterina Morozova. We gratefully acknowledge helpful conversations with
962 Paul Miller, Mark Zielinski, Sriram Sampath and Alec Hoyland.

963 This work was funded by NIH grants T32 NS007292 (SGS) and R35 NS097343 (EM and SGS), NIH
964 MH060605 (FN and DB) and DFG SCHN 1594/1-1 (ACS).

965 References

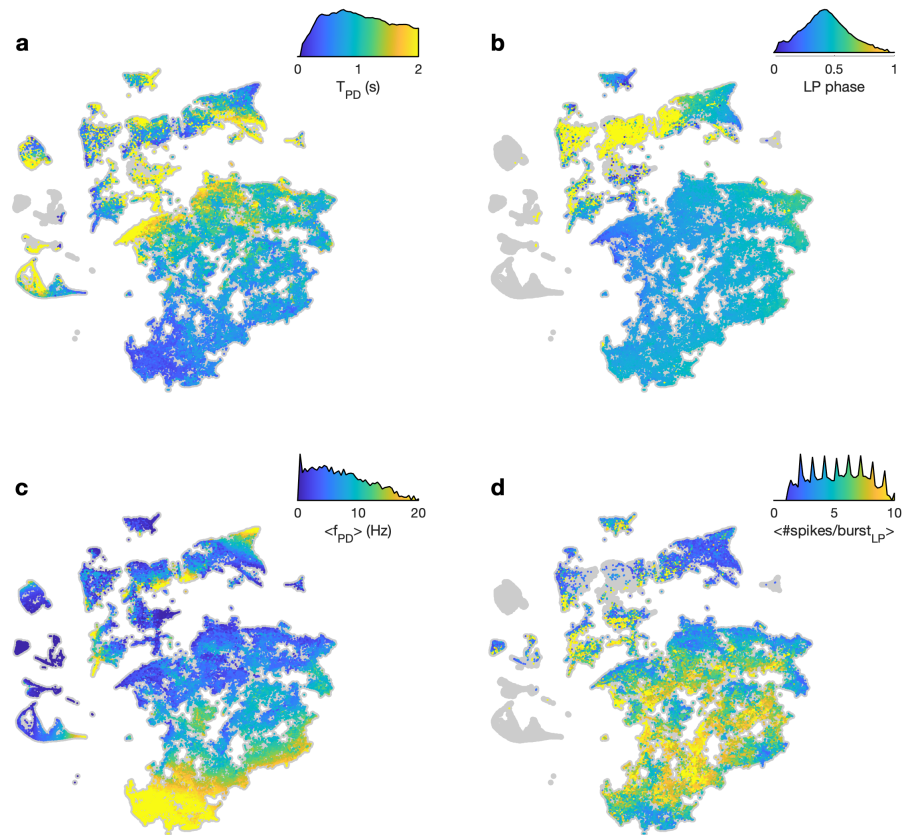
- 966 **Allen M**, Poggiali D, Whitaker K, Marshall TR, Kievit RA. Raincloud plots: a multi-platform tool for robust data
967 visualization. Wellcome open research. 2019; 4.
- 968 **Alonso LM**, Marder E. Visualization of currents in neural models with similar behavior and different conductance
969 densities. eLife. 2019; 8:e42722.
- 970 **Alonso LM**, Marder E. Temperature compensation in a small rhythmic circuit. eLife. 2020; 9:e55470.
- 971 **Bal T**, Nagy F, Moulins M. Muscarinic modulation of a pattern-generating network: control of neuronal properties.
972 Journal of Neuroscience. 1994; 14(5):3019–3035.
- 973 **Baldi P**. Autoencoders, unsupervised learning, and deep architectures. In: *Proceedings of ICML workshop on*
974 *unsupervised and transfer learning* JMLR Workshop and Conference Proceedings; 2012. p. 37–49.
- 975 **Beltz B**, Eisen JS, Flamm R, Harris-Warrick R, Hooper SL, Marder E. Serotonergic innervation and modulation of
976 the stomatogastric ganglion of three decapod crustaceans (*Panulirus interruptus*, *Homarus americanus* and
977 *Cancer irroratus*). Journal of experimental biology. 1984; 109(1):35–54.
- 978 **Berman GJ**, Choi DM, Bialek WS, Shaevitz JW. Mapping the stereotyped behaviour of freely moving fruit flies.
979 Journal of the Royal Society Interface. 2014 Oct; 11(99):20140672–20140672.
- 980 **Böhm JN**, Berens P, Kobak D. A Unifying Perspective on Neighbor Embeddings along the Attraction-Repulsion
981 Spectrum. arXiv preprint arXiv:200708902. 2020; .
- 982 **Börner K**, Chen C, Boyack KW. Visualizing knowledge domains. Annual review of information science and
983 technology. 2003; 37(1):179–255.
- 984 **Brunel N**, Wang XJ. What determines the frequency of fast network oscillations with irregular neural discharges?
985 I. Synaptic dynamics and excitation-inhibition balance. Journal of Neurophysiology. 2003; 90(1):415–430.
- 986 **Bucher D**, Prinz AA, Marder E. Animal-to-animal variability in motor pattern production in adults and during
987 growth. Journal of Neuroscience. 2005 Feb; 25(7):1611–1619.
- 988 **Caplan JS**, Williams AH, Marder E. Many Parameter Sets in a Multicompartment Model Oscillator Are Robust to
989 Temperature Perturbations. Journal of Neuroscience. 2014 Apr; 34(14):4963–4975.
- 990 **Chen W**, Zhao Y, Chen X, Yang Z, Xu X, Bi Y, Chen V, Li J, Choi H, Ernest B, Tran B, Mehta M, Kumar P, Farmer A, Mir
991 A, Mehra UA, Li JL, Moos M, Xiao W, Wang C. A multicenter study benchmarking single-cell RNA sequencing
992 technologies using reference samples. Nature Biotechnology. 2020 Dec; p. 1–29.
- 993 **Christen M**, Kohn A, Ott T, Stoop R. Measuring spike pattern reliability with the Lempel-Ziv-distance. Journal of
994 Neuroscience Methods. 2006; 156(1-2):342–350.
- 995 **Clark DG**, Livezey JA, Bouchard KE. Unsupervised Discovery of Temporal Structure in Noisy Data with Dynamical
996 Components Analysis. arXiv. 2019 May; .
- 997 **Clark MC**. Arthropod 5-HT₂ Receptors: A Neurohormonal Receptor in Decapod Crustaceans That Displays Ago-
998 nist Independent Activity Resulting from an Evolutionary Alteration to the DRY Motif. Journal of Neuroscience.
999 2004 Mar; 24(13):3421–3435.
- 1000 **Clemens S**, Massabuau JC, Meyrand P, Simmers J. A modulatory role for oxygen in shaping rhythmic motor
1001 output patterns of neuronal networks. Respir Physiol. 2001 Nov; 128(3):299–315.
- 1002 **Corver A**, Wilkerson N, Miller J, Gordus AG. Distinct movement patterns generate stages of spider web-building.
1003 bioRxiv. 2021; .
- 1004 **Cox MA**, Cox TF. Multidimensional scaling. In: *Handbook of data visualization* Springer; 2008.p. 315–347.
- 1005 **Cunningham JP**, Yu BM. Dimensionality reduction for large-scale neural recordings. Nature Neuroscience. 2014
1006 Aug; 17(11):1500–1509.
- 1007 **Cymbalyuk GS**, Gaudry Q, Masino MA, Calabrese RL. Bursting in leech heart interneurons: cell-autonomous
1008 and network-based mechanisms. Journal of Neuroscience. 2002 Dec; 22(24):10580–10592.
- 1009 **Daur N**, Nadim F, Bucher D. The complexity of small circuits: the stomatogastric nervous system. Current
1010 Opinion in Neurobiology. 2016; 41:1–7.

- 1011 **Dickinson PS**, Hauptman J, Hetling J, Mahadevan A. RPCH modulation of a multi-oscillator network: effects on
1012 the pyloric network of the spiny lobster. *Journal of Neurophysiology*. 2001; 85(4):1424–1435.
- 1013 **Dimitriadis G**, Neto JP, Kampff AR. t-SNE Visualization of Large-Scale Neural Recordings. *Neural Computation*.
1014 2018 Jun; 30(7):1750–1774.
- 1015 **Eisen JS**, Marder E. A mechanism for production of phase shifts in a pattern generator. *Journal of neurophysiol-*
1016 *ogy*. 1984; 51(6):1375–1393.
- 1017 **Eisen JS**, Marder E. Mechanisms underlying pattern generation in lobster stomatogastric ganglion as determined
1018 by selective inactivation of identified neurons. III. Synaptic connections of electrically coupled pyloric neurons.
1019 *Journal of Neurophysiology*. 1982; 48(6):1392–1415.
- 1020 **Epstein I**, Marder E. Multiple modes of a conditional neural oscillator. *Biological cybernetics*. 1990; 63(1):25–34.
- 1021 **Fortuin V**, Hüser M, Locatello F, Strathmann H, Rättsch G. SOM-VAE: Interpretable Discrete Representation
1022 Learning on Time Series. *arXiv*. 2018 Jun; .
- 1023 **Franci A**, O’Leary T, Golowasch J. Positive dynamical networks in neuronal regulation: how tunable variability
1024 coexists with robustness. *IEEE Control Systems Letters*. 2020; .
- 1025 **Frankel NW**, Pontius W, Dufour YS, Long J, Hernandez-Nunez L, Emonet T. Adaptability of non-genetic diversity
1026 in bacterial chemotaxis. *eLife*. 2014; 3:e03526.
- 1027 **Garcia VJ**, Daur N, Temporal S, Schulz DJ, Bucher D. Neuropeptide Receptor Transcript Expression Levels and
1028 Magnitude of Ionic Current Responses Show Cell Type-Specific Differences in a Small Motor Circuit. *Journal of*
1029 *Neuroscience*. 2015 Apr; 35(17):6786–6800.
- 1030 **Golowasch J**, Marder E. Proctolin activates an inward current whose voltage dependence is modified by
1031 extracellular Ca^{2+} . *Journal of Neuroscience*. 1992 Mar; 12(3):810–817.
- 1032 **Golowasch J**, Casey M, Abbott L, Marder E. Network Stability from Activity-Dependent Regulation of Neuronal
1033 Conductances. *Neural Computation*. 1999 Jul; 11(5):1079–1096.
- 1034 **Golowasch J**, Goldman MS, Abbott L, Marder E. Failure of Averaging in the Construction of a Conductance-Based
1035 Neuron Model. *Journal of Neurophysiology*. 2002 Feb; 87(2):1129–1131.
- 1036 **Gonçalves PJ**, Lueckmann JM, Deistler M, Nonnenmacher M, Öcal K, Bassetto G, Chintaluri C, Podlaski WF,
1037 Haddad SA, Vogels TP, et al. Training deep neural density estimators to identify mechanistic models of neural
1038 dynamics. *eLife*. 2020; 9:e56261.
- 1039 **Gorur-Shandilya S**, Marder E, O’Leary T. Activity-dependent compensation of cell size is vulnerable to targeted
1040 deletion of ion channels. *Scientific Reports*. 2020; 10.
- 1041 **Gutierrez GJ**, Grashow RG. *Cancer borealis* stomatogastric nervous system dissection. *Journal of visualized*
1042 *experiments: JoVE*. 2009; (25).
- 1043 **Gutierrez GJ**, O’Leary T, Marder E. Multiple mechanisms switch an electrically coupled, synaptically inhibited
1044 neuron between competing rhythmic oscillators. *Neuron*. 2013; 77(5):845–858.
- 1045 **Haddad SA**, Marder E. Circuit Robustness to Temperature Perturbation Is Altered by Neuromodulators. *Neuron*.
1046 2018 Nov; 100(3):609–623.
- 1047 **Haley JA**, Hampton D, Marder E. Two central pattern generators from the crab, *Cancer borealis*, respond robustly
1048 and differentially to extreme extracellular pH. *eLife*. 2018 Dec; 7:e41877.
- 1049 **Hamood AW**, Haddad SA, Otopalik AG, Rosenbaum P, Marder E. Quantitative Reevaluation of the Effects of
1050 Short- and Long-Term Removal of Descending Modulatory Inputs on the Pyloric Rhythm of the Crab, *Cancer*
1051 *borealis*. *eNeuro*. 2015 Jan; 2(1):1–13.
- 1052 **Hamood AW**, Marder E. Animal-to-Animal Variability in Neuromodulation and Circuit Function. *Cold Spring*
1053 *Harb Symp Quant Biol*. 2015 Jun; 79:21–28.
- 1054 **Harris-Warrick RM**, Flamm RE. Multiple mechanisms of bursting in a conditional bursting neuron. *Journal of*
1055 *Neuroscience*. 1987; 7(7):2113–2128.
- 1056 **Harris-Warrick RM**, Marder E. Modulation of neural networks for behavior. *Annual review of neuroscience*.
1057 1991; 14(1):39–57.

- 1058 **Hartline DK**, Maynard DM. Motor patterns in the stomatogastric ganglion of the lobster *Panulirus argus*. Journal
1059 of Experimental Biology. 1975; 62(2):405–420.
- 1060 **He LS**, Rue MC, Morozova EO, Powell DJ, James EJ, Kar M, Marder E. Rapid adaptation to elevated extracellular
1061 potassium in the pyloric circuit of the crab, *Cancer borealis*. Journal of Neurophysiology. 2020; 123(5):2075–
1062 2089.
- 1063 **Hooper SL**, Marder E. Modulation of a central pattern generator by two neuropeptides, proctolin and FMR-
1064 Famide. Brain Research. 1984 Jul; 305(1):186–191.
- 1065 **Hooper SL**, Marder E. Modulation of the lobster pyloric rhythm by the peptide proctolin. Journal of Neuroscience.
1066 1987; 7(7):2097–2112.
- 1067 **Hooper SL**, Thuma JB, Guschlbauer C, Schmidt J, Büschges A. Cell dialysis by sharp electrodes can cause
1068 nonphysiological changes in neuron properties. Journal of Neurophysiology. 2015; 114(2):1255–1271.
- 1069 **Kobak D**, Berens P. The art of using t-SNE for single-cell transcriptomics. Nature Communications. 2019 Nov; p.
1070 1–14.
- 1071 **Kobak D**, Linderman GC. Initialization is critical for preserving global data structure in both t-SNE and UMAP.
1072 Nature biotechnology. 2021; 39(2):156–157.
- 1073 **Kollmorgen S**, Hahnloser RH, Mante V. Nearest neighbours reveal fast and slow components of motor learning.
1074 Nature. 2020; 577(7791):526–530.
- 1075 **Kushinsky D**, Morozova EO, Marder E. In vivo effects of temperature on the heart and pyloric rhythms in the
1076 crab *Cancer borealis*. Journal of Experimental Biology. 2019; 222(5).
- 1077 **Kyriazi P**, Headley DB, Pare D. Multi-dimensional Coding by Basolateral Amygdala Neurons. Neuron. 2018 Sep;
1078 99(6):1315–1328.e5.
- 1079 **Leelatian N**, Sinnaeve J, Mistry AM, Barone SM, Brockman AA, Diggins KE, Greenplate AR, Weaver KD, Thompson
1080 RC, Chambless LB, Mobley BC, Ihrie RA, Irish JM. Unsupervised machine learning reveals risk stratifying
1081 glioblastoma tumor cells. eLife. 2020 Jun; 9:545.
- 1082 **Linderman GC**, Rachh M, Hoskins JG, Steinerberger S, Kluger Y. Fast interpolation-based t-SNE for improved
1083 visualization of single-cell RNA-seq data. Nature methods. 2019; 16(3):243–245.
- 1084 **Linderman GC**, Steinerberger S. Clustering with t-SNE, provably. SIAM Journal on Mathematics of Data Science.
1085 2019; 1(2):313–332.
- 1086 **Van der Maaten L**, Hinton G. Visualizing data using t-SNE. Journal of machine learning research. 2008; 9(11).
- 1087 **Mackevicius EL**, Bahle AH, Williams AH, Gu S, Denisenko NI, Goldman MS, Fee MS. Unsupervised discovery of
1088 temporal sequences in high-dimensional datasets, with applications to neuroscience. eLife. 2019; 8:e38471.
- 1089 **Macosko EZ**, Basu A, Satija R, Nemes J, Shekhar K, Goldman M, Tirosh I, Bialas AR, Kamitaki N, Martersteck EM,
1090 Trombetta JJ, Weitz DA, Sanes JR, Shalek AK, Regev A, McCarroll SA. Highly Parallel Genome-wide Expression
1091 Profiling of Individual Cells Using Nanoliter Droplets. Cell. 2015 May; 161(5):1202–1214.
- 1092 **Madiraju NS**, Sadat SM, Fisher D, Karimabadi H. Deep Temporal Clustering : Fully Unsupervised Learning of
1093 Time-Domain Features. arXiv. 2018 Feb; .
- 1094 **Marbán E**. Cardiac channelopathies. Nature. 2002 Jan; 415(6868):213–218.
- 1095 **Marder E**. Neuromodulation of neuronal circuits: back to the future. Neuron. 2012; 76(1):1–11.
- 1096 **Marder E**, Bucher D. Understanding circuit dynamics using the stomatogastric nervous system of lobsters and
1097 crabs. Annu Rev Physiol. 2007; 69:291–316.
- 1098 **Marder E**, Hooper SL. Neurotransmitter modulation of the stomatogastric ganglion of decapod crustaceans. In:
1099 *Model neural networks and behavior* Springer; 1985.p. 319–337.
- 1100 **Marder E**, Hooper SL, Siwicki KK. Modulatory action and distribution of the neuropeptide proctolin in the
1101 crustacean stomatogastric nervous system. Journal of Comparative Neurology. 1986; 243(4):454–467.
- 1102 **Marder E**, Weimann JM. Modulatory control of multiple task processing in the stomatogastric nervous system.
1103 In: *Neurobiology of motor programme selection* Elsevier; 1992.p. 3–19.

- 1104 **Mariño J**, Schummers J, Lyon DC, Schwabe L, Beck O, Wiesing P, Obermayer K, Sur M. Invariant computations in
1105 local cortical networks with balanced excitation and inhibition. *Nature neuroscience*. 2005; 8(2):194–201.
- 1106 **Miller JP**, Selverston AI. Mechanisms underlying pattern generation in lobster stomatogastric ganglion as
1107 determined by selective inactivation of identified neurons. IV. Network properties of pyloric system. *Journal*
1108 *of neurophysiology*. 1982; 48(6):1416–1432.
- 1109 **Mizrahi A**, Dickinson PS, Kloppenburg P, Fénelon V, Baro DJ, Harris-Warrick RM, Meyrand P, Simmers J. Long-
1110 term maintenance of channel distribution in a central pattern generator neuron by neuromodulatory inputs
1111 revealed by decentralization in organ culture. *Journal of Neuroscience*. 2001; 21(18):7331–7339.
- 1112 **Moor M**, Horn M, Rieck B, Borgwardt K. Topological Autoencoders. arXiv. 2019 Jun; .
- 1113 **Nguyen LH**, Holmes S. Ten quick tips for effective dimensionality reduction. *PLoS Computational Biology*. 2019
1114 Jun; 15(6):e1006907–19.
- 1115 **Nusbaum MP**, Marder E. A Neuronal Role for a Crustacean Red Pigment Concentrating Hormone-like Peptide:
1116 Neuromodulation of the Pyloric Rhythm in the Crab, *Cancer borealis*. *Journal of Experimental Biology*. 1988
1117 Sep; 135:1–17.
- 1118 **Nusbaum MP**, Marder E. A modulatory proctolin-containing neuron (MPN). I. Identification and characterization.
1119 *Journal of Neuroscience*. 1989; 9(5):1591–1599.
- 1120 **O’Leary T**, Williams AH, Franci A, Marder E. Cell Types, Network Homeostasis, and Pathological Compensation
1121 from a Biologically Plausible Ion Channel Expression Model. *Neuron*. 2014 May; 82(4):809–821.
- 1122 **Pang R**, Lansdell BJ, Fairhall AL. Dimensionality reduction in neuroscience. *Current Biology*. 2016 Jul; 26(14):R656–
1123 60.
- 1124 **Peacock JA**. Two-dimensional goodness-of-fit testing in astronomy. *Monthly Notices of the Royal Astronomical*
1125 *Society*. 1983; 202(3):615–627.
- 1126 **Powell D**, Haddad SA, Gorur-Shandilya S, Marder E. Coupling between fast and slow oscillator circuits in *Cancer*
1127 *borealis* is temperature-compensated. *eLife*. 2021; 10:e60454.
- 1128 **Prinz AA**, Billimoria CP, Marder E. Alternative to Hand-Tuning Conductance-Based Models: Construction and
1129 Analysis of Databases of Model Neurons. *Journal of Neurophysiology*. 2003 Dec; 90(6):3998–4015.
- 1130 **Prinz AA**, Bucher D, Marder E. Similar network activity from disparate circuit parameters. *Nature Neuroscience*.
1131 2004 Nov; 7(12):1345–1352.
- 1132 **Qadri SA**, Camacho J, Wang H, Taylor JR, Grosell M, Worden MK. Temperature and acid–base balance in the
1133 American lobster *Homarus americanus*. *Journal of Experimental Biology*. 2007; 210(7):1245–1254.
- 1134 **Ratliff J**, Franci A, Marder E, O’Leary T. Neuronal oscillator robustness to multiple global perturbations. *Biophys-*
1135 *ical Journal*. 2021; .
- 1136 **Rinberg A**, Taylor AL, Marder E. The effects of temperature on the stability of a neuronal oscillator. *PLoS*
1137 *Computational Biology*. 2013; 9(1):e1002857.
- 1138 **Rosenbaum P**, Marder E. Graded Transmission without Action Potentials Sustains Rhythmic Activity in Some
1139 But Not All Modulators That Activate the Same Current. *Journal of Neuroscience*. 2018 Oct; 38(42):8976–8988.
- 1140 **Rossum Mv**. A novel spike distance. *Neural computation*. 2001; 13(4):751–763.
- 1141 **Rumelhart DE**, Hinton GE, Williams RJ. Learning internal representations by error propagation. *California Univ*
1142 *San Diego La Jolla Inst for Cognitive Science*; 1985.
- 1143 **Russell DF**. Rhythmic excitatory inputs to the lobster stomatogastric ganglion. *Brain research*. 1976; 101(3):582–
1144 588.
- 1145 **Schreiber S**, Fellous JM, Whitmer D, Tiesinga P, Sejnowski TJ. A new correlation-based measure of spike timing
1146 reliability. *Neurocomputing*. 2003; 52:925–931.
- 1147 **Schulz DJ**, Goillard JM, Marder E. Variable channel expression in identified single and electrically coupled
1148 neurons in different animals. *Nature neuroscience*. 2006; 9(3):356–362.

- 1149 **Schulz DJ**, Goillard JM, Marder EE. Quantitative expression profiling of identified neurons reveals cell-specific
1150 constraints on highly variable levels of gene expression. *Proceedings of the National Academy of Sciences*.
1151 2007; 104(32):13187–13191.
- 1152 **Settles B**. Active learning literature survey. Doctoral Dissertation, University of Wisconsin-Madison. 2009; .
- 1153 **Shneiderman B**, Wattenberg M. Ordered treemap layouts. In: *IEEE Symposium on Information Visualization*,
1154 2001. *INFOVIS 2001*. IEEE; 2001. p. 73–78.
- 1155 **Spitzer N**, Cymbalyuk G, Zhang H, Edwards DH, Baro DJ. Serotonin Transduction Cascades Mediate Variable
1156 Changes in Pyloric Network Cycle Frequency in Response to the Same Modulatory Challenge. *Journal of*
1157 *Neurophysiology*. 2008 Jun; 99(6):2844–2863.
- 1158 **Staley K**. Molecular mechanisms of epilepsy. *Nature Neuroscience*. 2015 Feb; 18(3):367–372.
- 1159 **Swensen AM**, Marder E. Multiple peptides converge to activate the same voltage-dependent current in a central
1160 pattern-generating circuit. *Journal of Neuroscience*. 2000; 20(18):6752–6759.
- 1161 **Swensen AM**, Marder E. Modulators with Convergent Cellular Actions Elicit Distinct Circuit Outputs. *Journal of*
1162 *Neuroscience*. 2001 Jun; 21(11):4050–4058.
- 1163 **Tang LS**, Taylor AL, Rinberg A, Marder E. Robustness of a Rhythmic Circuit to Short- and Long-Term Temperature
1164 Changes. *Journal of Neuroscience*. 2012 Jul; 32(29):10075–10085.
- 1165 **Tang LS**, Goeritz ML, Caplan JS, Taylor AL, Fişek M, Marder E. Precise Temperature Compensation of Phase in a
1166 Rhythmic Motor Pattern. *PLoS Biology*. 2010 Aug; 8(8):e1000469.
- 1167 **Thirumalai V**, Marder E. Colocalized Neuropeptides Activate a Central Pattern Generator by Acting on Different
1168 Circuit Targets. *Journal of Neuroscience*. 2002 Mar; 22(5):1874–1882.
- 1169 **Thirumalai V**, Prinz AA, Johnson CD, Marder E. Red Pigment Concentrating Hormone Strongly Enhances the
1170 Strength of the Feedback to the Pyloric Rhythm Oscillator But Has Little Effect on Pyloric Rhythm Period.
1171 *Journal of Neurophysiology*. 2006 Mar; 95(3):1762–1770.
- 1172 **Thoby-Brisson M**, Simmers J. Neuromodulatory inputs maintain expression of a lobster motor pattern-
1173 generating network in a modulation-dependent state: evidence from long-term decentralization *in vitro*.
1174 *Journal of Neuroscience*. 1998; 18(6):2212–2225.
- 1175 **Timme M**. Revealing network connectivity from response dynamics. *Physical review letters*. 2007; 98(22):224101.
- 1176 **Tobin AE**, Cruz-Bermúdez ND, Marder E, Schulz DJ. Correlations in ion channel mRNA in rhythmically active
1177 neurons. *PloS one*. 2009; 4(8):e6742.
- 1178 **Turrigiano G**, Abbott L, Marder E. Activity-dependent changes in the intrinsic properties of cultured neurons.
1179 *Science*. 1994 May; 264(5161):974–977.
- 1180 **Turrigiano G**, LeMasson G, Marder E. Selective regulation of current densities underlies spontaneous changes
1181 in the activity of cultured neurons. *Journal of Neuroscience*. 1995 May; 15(5):3640–3652.
- 1182 **Turrigiano GG**, Marder E. Modulation of identified stomatogastric ganglion neurons in primary cell culture.
1183 *Journal of Neurophysiology*. 1993 Jun; 69(6):1993–2002.
- 1184 **Victor JD**, Purpura KP. Metric-space analysis of spike trains: theory, algorithms and application. *Network:*
1185 *computation in neural systems*. 1997; 8(2):127–164.
- 1186 **van Vreeswijk C**, Sompolinsky H. Chaos in neuronal networks with balanced excitatory and inhibitory activity.
1187 *Science*. 1996 Dec; 274(5293):1724–1726.
- 1188 **Vyas S**, Golub MD, Sussillo D, Shenoy KV. Computation Through Neural Population Dynamics. *Annual Reviews*
1189 *of Neuroscience*. 2020 Jul; 43(1):249–275.
- 1190 **Weimann JM**, Marder E. Switching neurons are integral members of multiple oscillatory networks. *Current*
1191 *Biology*. 1994; 4(10):896–902.
- 1192 **Williams AH**, Degleris A, Wang Y, Linderman SW. Point process models for sequence detection in high-
1193 dimensional neural spike trains. *arXiv*. 2020 Oct; .
- 1194 **Williams AH**, Kim TH, Wang F, Vyas S, Ryu SI, Shenoy KV, Schnitzer M, Kolda TG, Ganguli S. Unsupervised
1195 Discovery of Demixed, Low- Dimensional Neural Dynamics across Multiple Timescales through Tensor
1196 Component Analysis. *Neuron*. 2018 Jun; 98(6):1099–1115.e8.



1197

Figure 2-Figure supplement 1. Burst metrics smoothly vary in map. In each panel, embedding of the entire dataset is shown in gray. Points are colored by (a) burst period of the PD neuron (b) phase of LP burst start in PD time (c) mean firing rate of PD neuron and (d) mean number of spikes per burst in the LP neuron. In each panel, the color scale also shows the distribution of metric over the entire data set (Y-axis in log scale). The distribution in (d) is spiky because the mean number of spikes/burst tends to be integer valued.

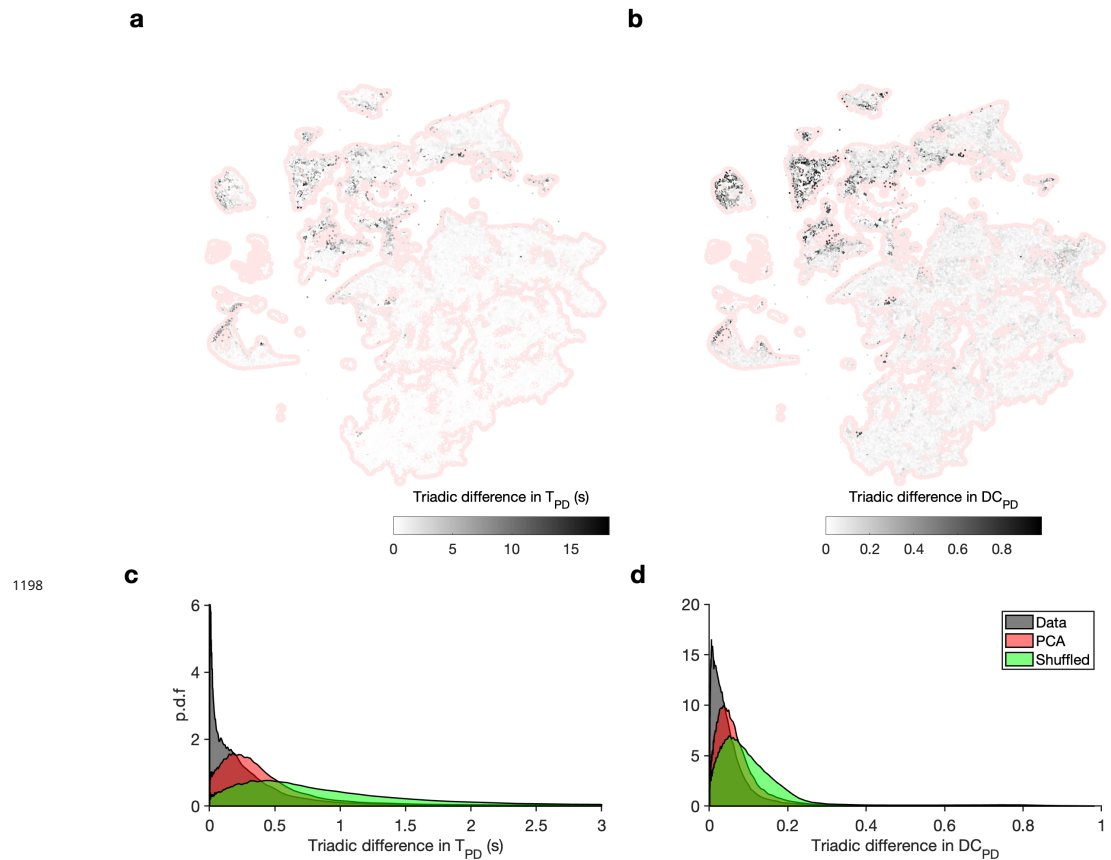


Figure 2-Figure supplement 2. Embedding arranges data so that neighbors tend to be similar. (a) Map shows embedding of all data in red shading. Shaded dots are incenters of a Delaunay triangulation of the map, and shading indicates the maximum absolute value of difference between burst period of the PD neuron in each cell in the triangulation. (b) Distribution of absolute triadic differences over the entire dataset (gray), compared to triadic differences between shuffled triads (green) and compared to triadic differences between the first two principal components. Triadic differences are significantly smaller than in the shuffled data and in the principal components ($p < .001$, K-S test). (c-d) Same as in (a-b), for the duty cycle of the PD neuron.

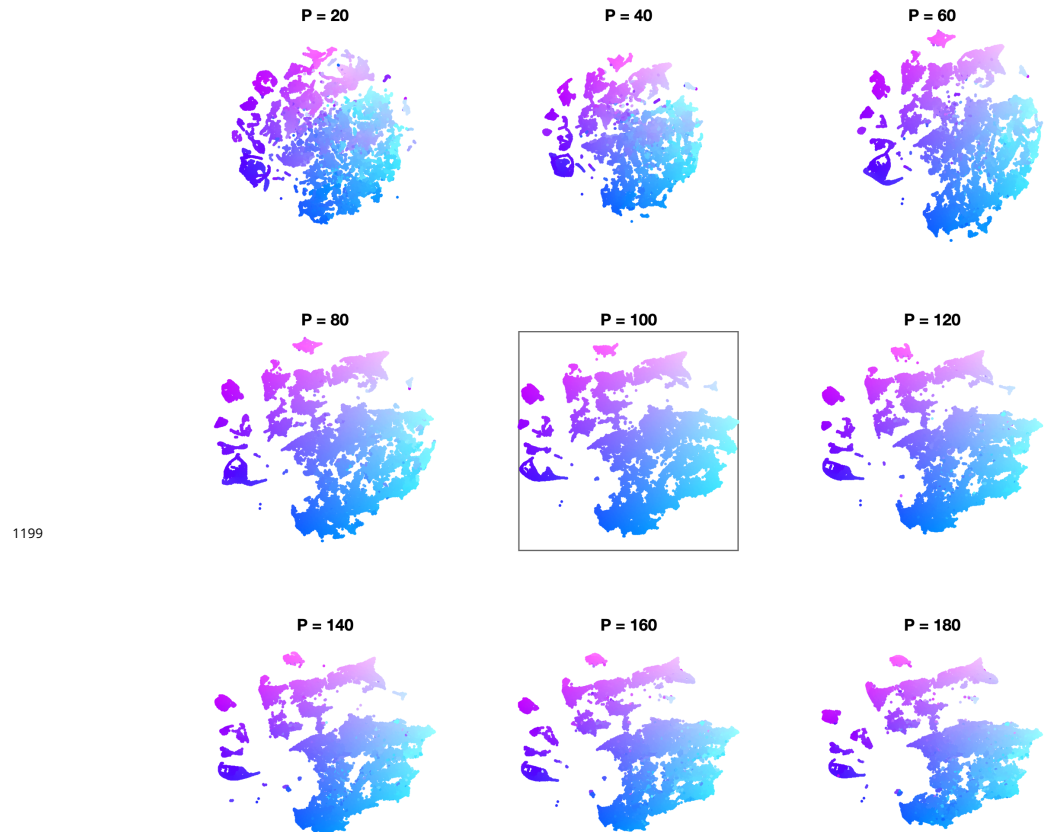


Figure 2-Figure supplement 3. Effect of varying perplexity in t-SNE embedding. In each panel, data are embedded using t-SNE using the indicated perplexity parameter. Initialization is the same across all perplexities (Methods and Materials). In every panel, points are colored by their location in the embedding with $P = 100$ (black box).

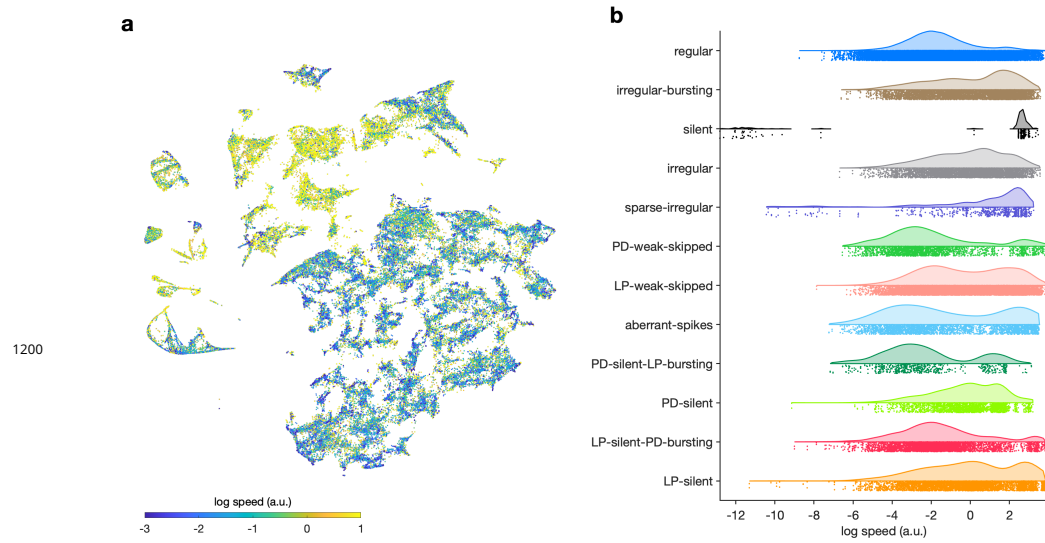
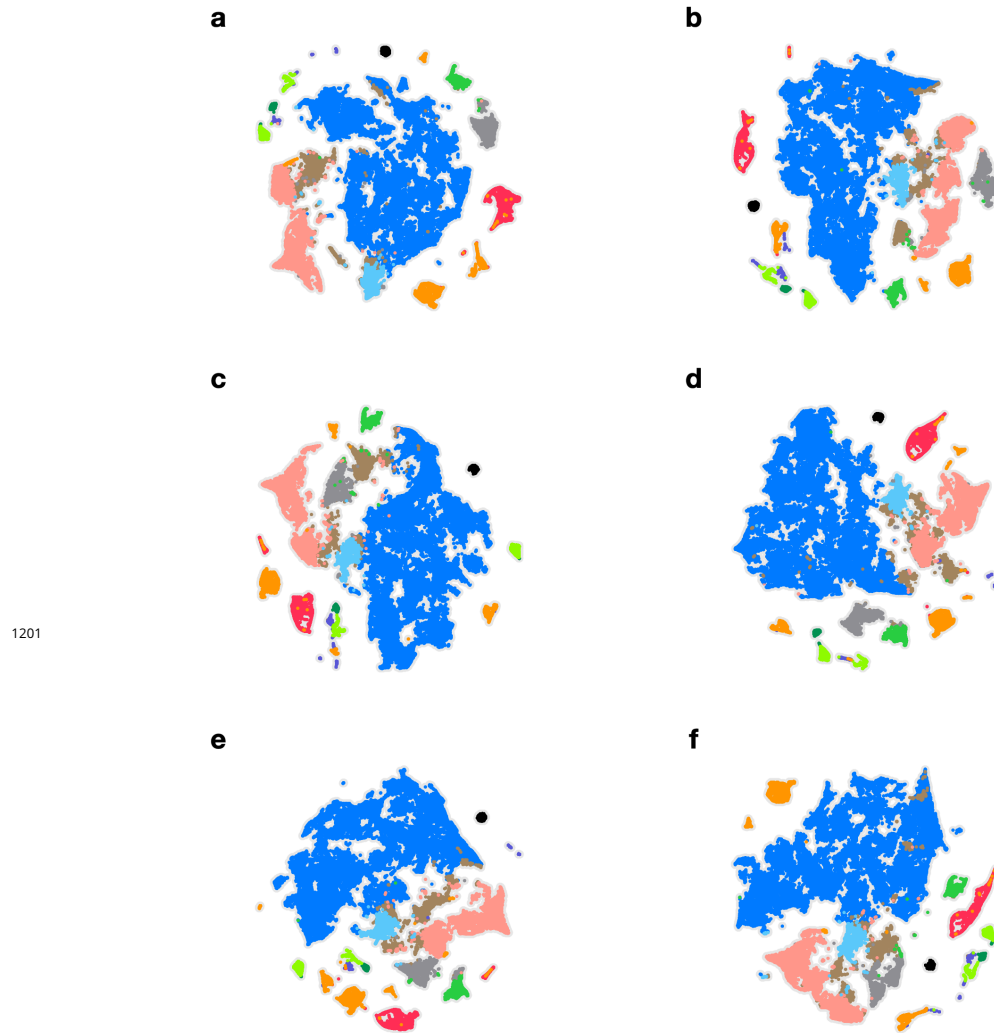


Figure 3-Figure supplement 1. Speed of trajectories through map. (a) Map colored by speed of trajectories through map at that point. Cooler colors indicate that preparations move through that region of space more slowly and warmer colors suggest that preparations are more likely to be far from that location in the next time step. (b) Speed grouped by manually identified labels.



1201

Figure 3-Figure supplement 2. Embeddings with different initializations. In each panel, the embedding is performed with a different initialization. (a-d) Random initializations. (e) Initializations based on minimum ISIs in PD and LP. (f) Initializations based on mean ISIs in PD and LP. In every panel, points are colored identically.

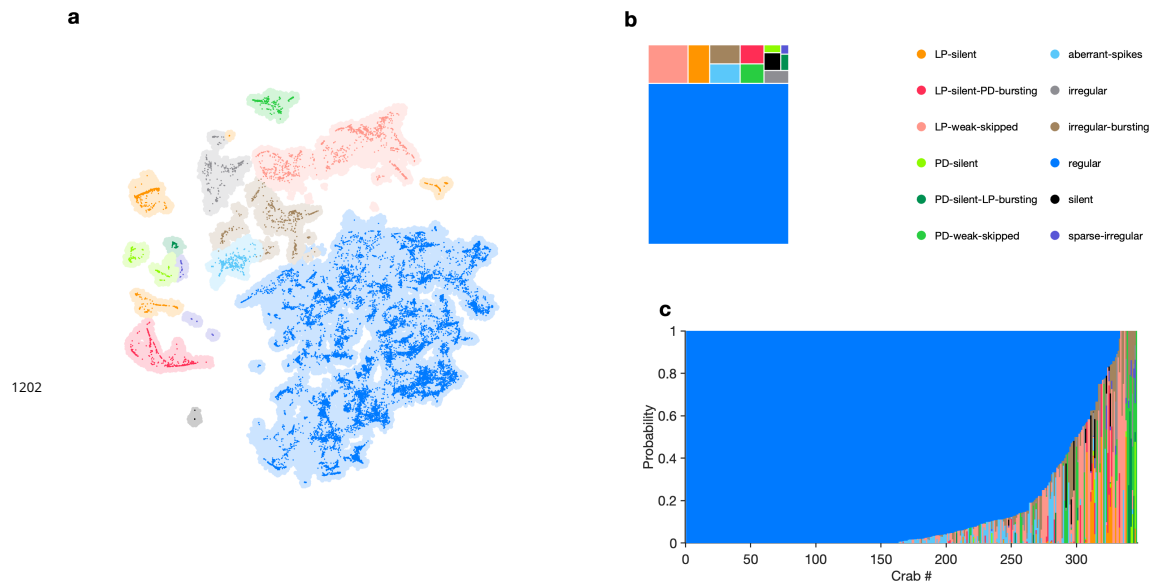


Figure 4-Figure supplement 1. State distribution under baseline conditions. (a) Map showing occupancy of baseline data. Shading indicates all data. Bright colored points are data from baseline conditions. (b) Treemap showing state probabilities under baseline conditions. (c) Preparation-by-preparation variation in state distribution under baseline conditions. $n = 22807$ data snippets from $N = 346$ individual preparations.

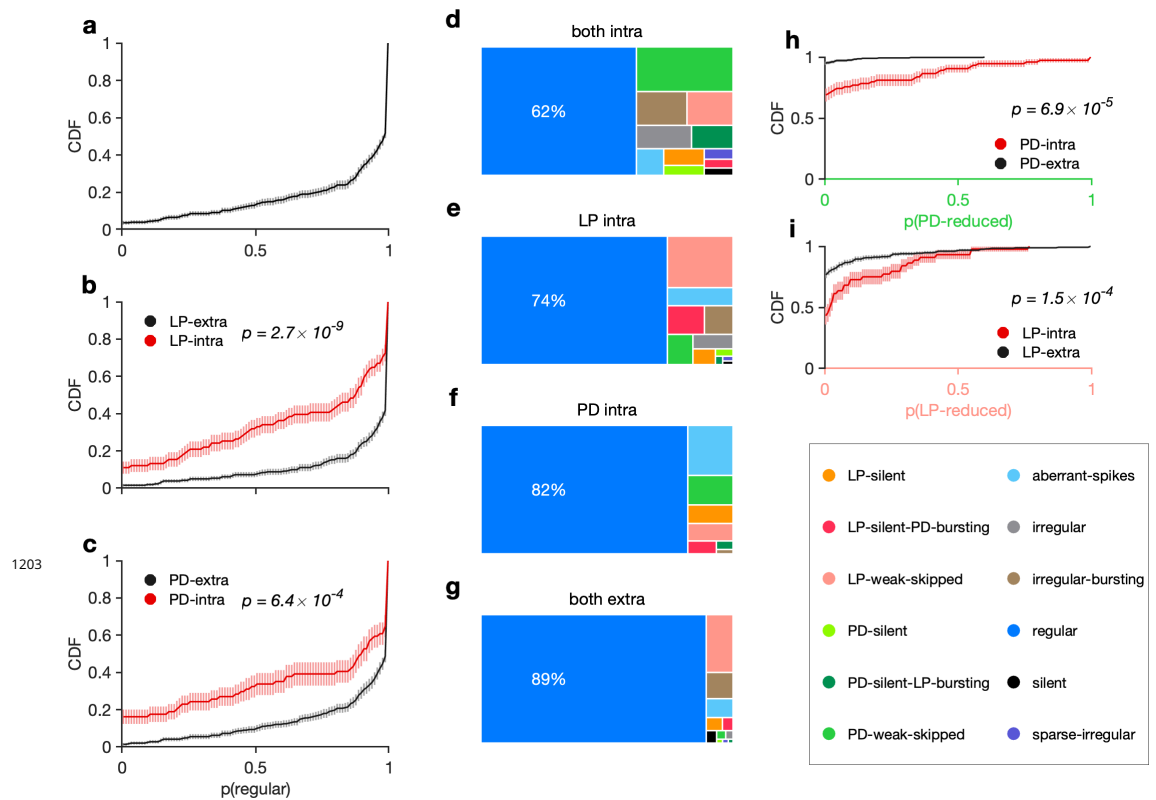


Figure 4-Figure supplement 2. Recording condition alters regular state probability. (a) Cumulative probability of the probability of observing a regular state, per animal. Cumulative probability of probability of regular state for preparations with LP (b) and PD (c) recorded extracellularly (black) vs. LP recorded intracellularly (red). (d-g) State probabilities in different recording conditions. (h) Probability of observing states in which PD activity is reduced (PD-silent, PD-weak-skipped) in preparations in which PD is recorded intracellularly (red) vs. preparations in which PD is recorded extracellularly (black). (i) Same as (h), but for LP. In all panels, thick lines show CDFs and shading indicates confidence intervals estimated by bootstrap. $n = 22807$, $N = 346$. p -values in each panel are from two-sample Kolmogorov-Smirnoff tests.

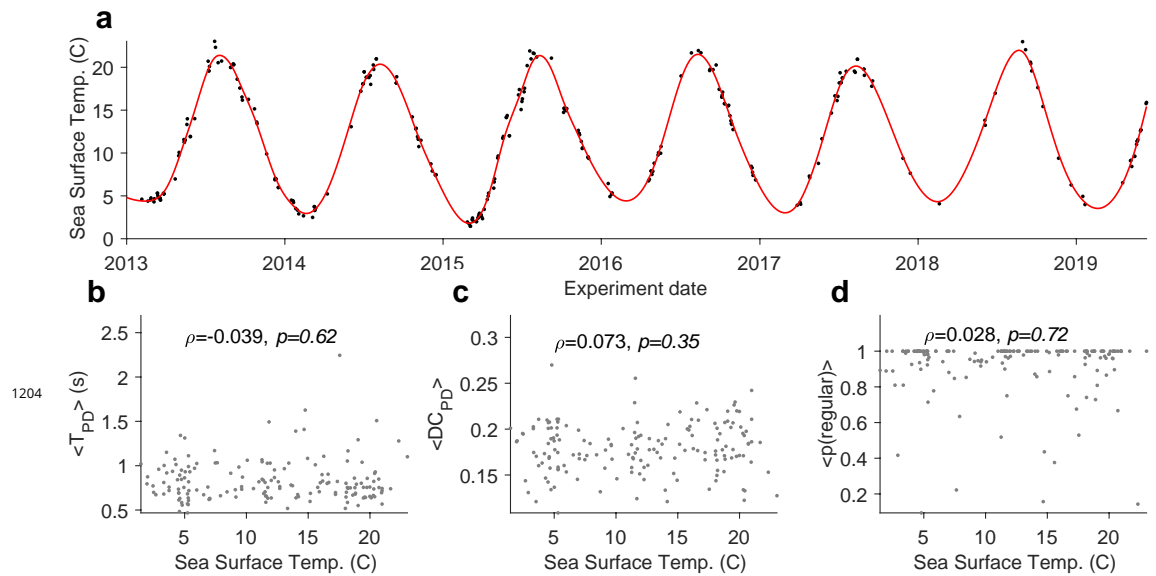


Figure 4-Figure supplement 3. Effect of sea surface temperature on baseline circuit dynamics. (a) Sea surface temperature at the Boston Harbor vs. experimental date. Red line is a smoothing fit. Mean burst period of PD neuron (b), mean duty cycle of PD (c), and probability of observing the regular state (d) vs. sea surface temperature. In all panels, each dot corresponds to a single preparation. $N = 312$ preparations. ρ is the Spearman correlation coefficient and p -value is from the Spearman rank correlation test.

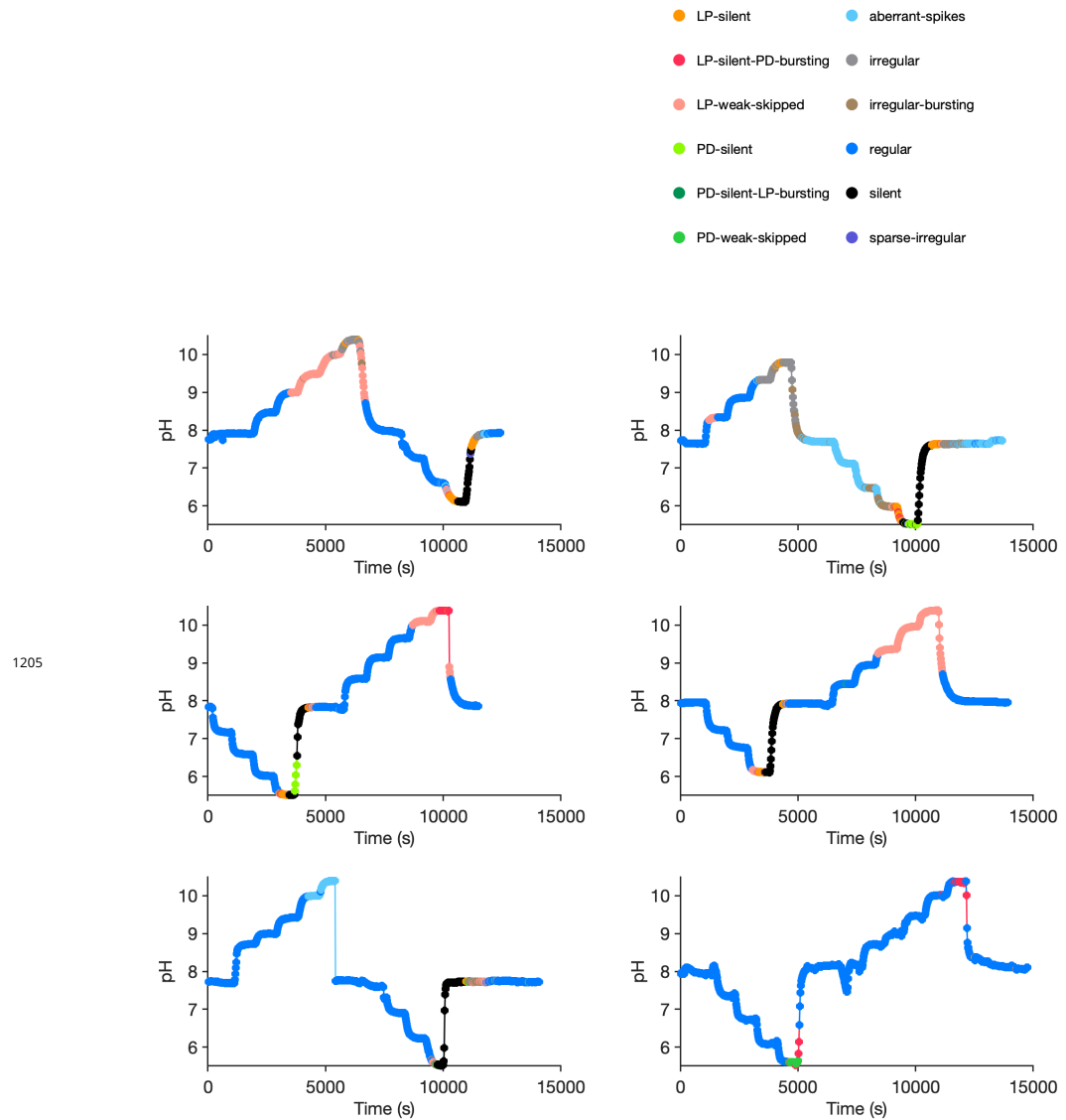


Figure 5-Figure supplement 1. Preparation-by-preparation response to pH perturbations. Each panel shows the response of a single preparation to pH perturbations. States are indicated in colors. Each preparation was stepped through various pH levels before returning to baseline pH. Note silent states (black) during acidic pH.

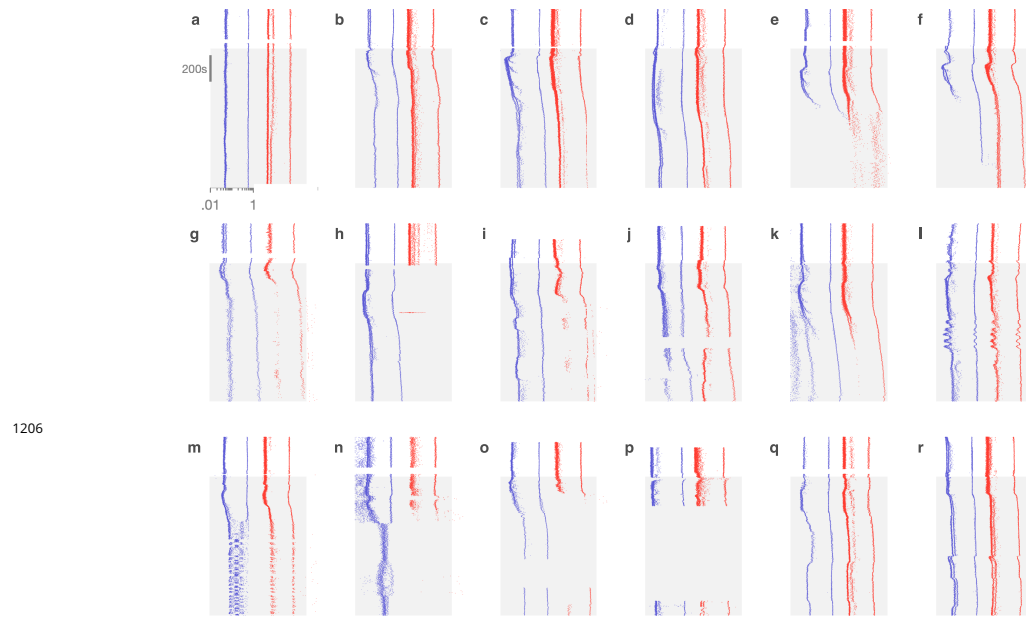


Figure 7-Figure supplement 1. Decentralization evokes variable dynamics. In each panel, inter-spike intervals (ISIs) of PD (blue) and LP are shown before and after (shaded) decentralization. The diversity of circuit responses to decentralization include minimal change (a), transient perturbation followed by recovery (b-d), silence in one or two neurons (e-h), slow oscillatory responses (l) and a switch from bursting to spiking (m,n). Each panel corresponds to a different preparation.

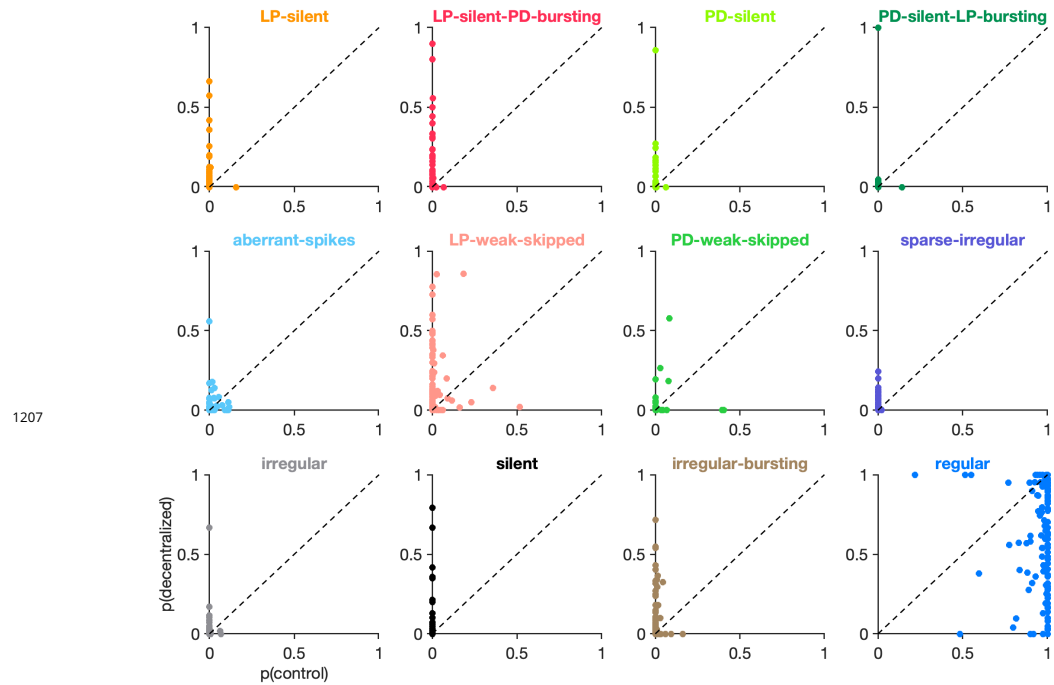


Figure 7-Figure supplement 2. Effects of decentralization on state probabilities. Each panel shows the probability of observing a given state before (x-axis) and after (y-axis) decentralization. Each dot is a single preparation. Probabilities computed on an animal-by-animal basis from $n = 16940$ points from $N = 140$ preparations.

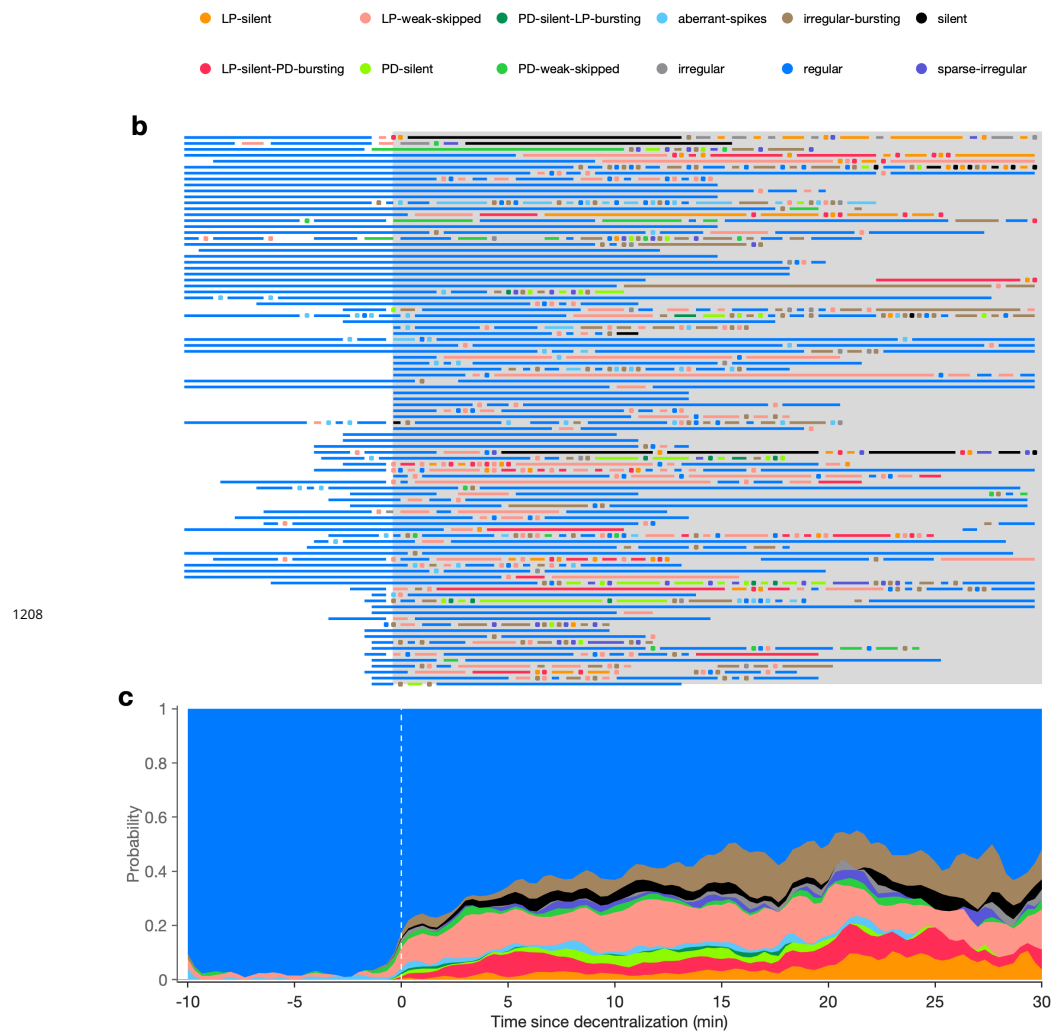


Figure 7-Figure supplement 3. Time course of effects of decentralization. (a) Each line shows the states exhibited by one circuit before and after (gray shaded region) decentralization. Dots indicate states that were maintained only for one time bin (20s). (b) Stacked bars show probabilities of displaying state vs. time. $N = 93$ animals.

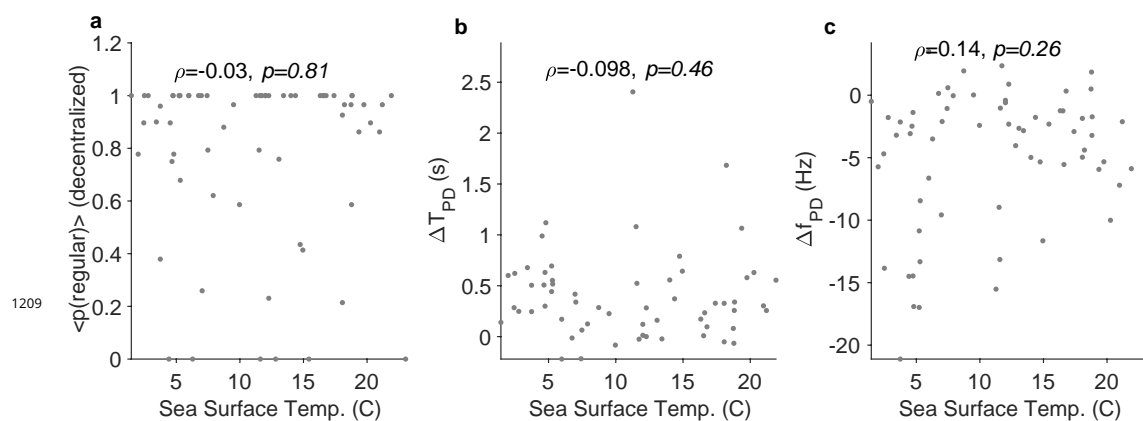


Figure 7-Figure supplement 4. Effects of decentralization do not correlate with seasonal effects. Probability of observing the *regular* state during decentralization (a), change in time period of PD neuron (b), and change in firing rate of PD (c) vs. sea surface temperature on day experiment was carried out. ρ is the Spearman correlation coefficient, and p -values are computed using the Spearman rank correlation test.

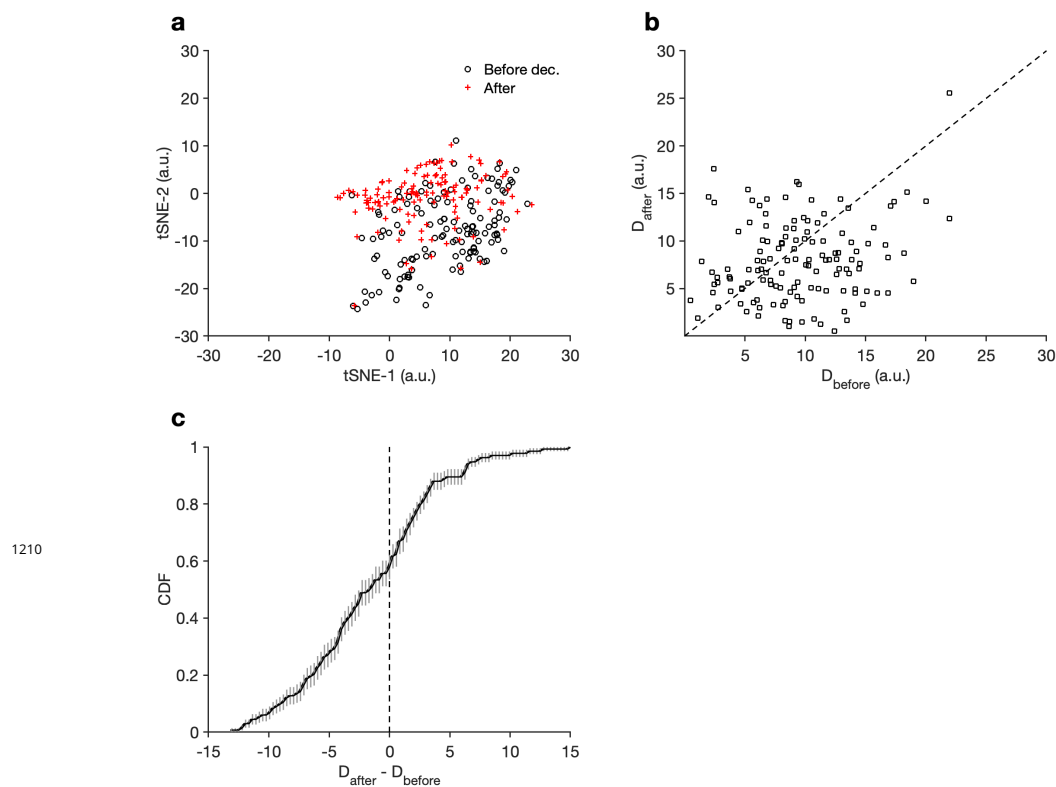


Figure 8-Figure supplement 1. Effects of decentralization on regular rhythms. (a) Mean locations of data in the *regular* cluster before and after decentralization. Each preparation is represented by a pair of points, one circle and one cross. (b) Dispersion (Methods and Materials) of data before and after decentralization. Each preparation is a single point. Note that the data appear to be skewed to the right, indicating larger dispersion before decentralization. (c) Distribution of differences in dispersion. The distribution of differences is not significantly skewed from a Gaussian ($p = .66$, Anderson-Darling test), and dispersion in decentralized preparations is significantly lower than in baseline ($p = .0016, t = 3.246$, paired t -test). $n = 13758$ points from $N = 140$ preparations.

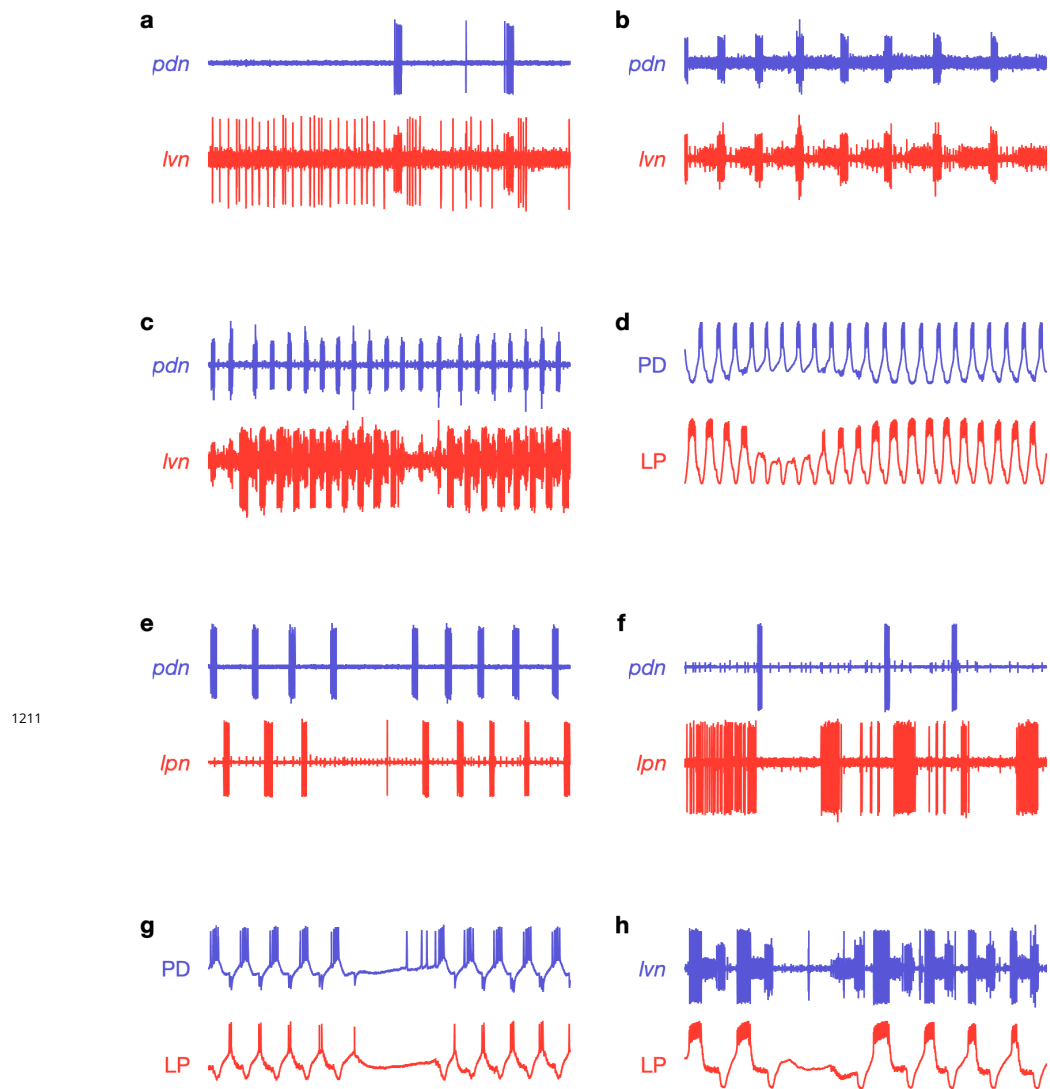


Figure 9-Figure supplement 1. Non-regular activity patterns in proctolin. Each panel shows a 20s snippet of raw recordings showing spikes from LP (red) and PD (blue). Each panel is from a different animal. Each row is from a different experimenter. (a) Irregular bursting, note prolonged spiking of LP on *lvn*. (b) LP completely silent, missing from *lvn*. (c) Intermittent LP interruptions, note breaks in *lvn*. (d) Interruption in LP bursting. (e) Interruption in PD and LP bursting. (f) Irregular bursting of both PD and LP. (g-h) Interruption of both PD and LP. Traces labelled PD or LP are intracellular recordings.

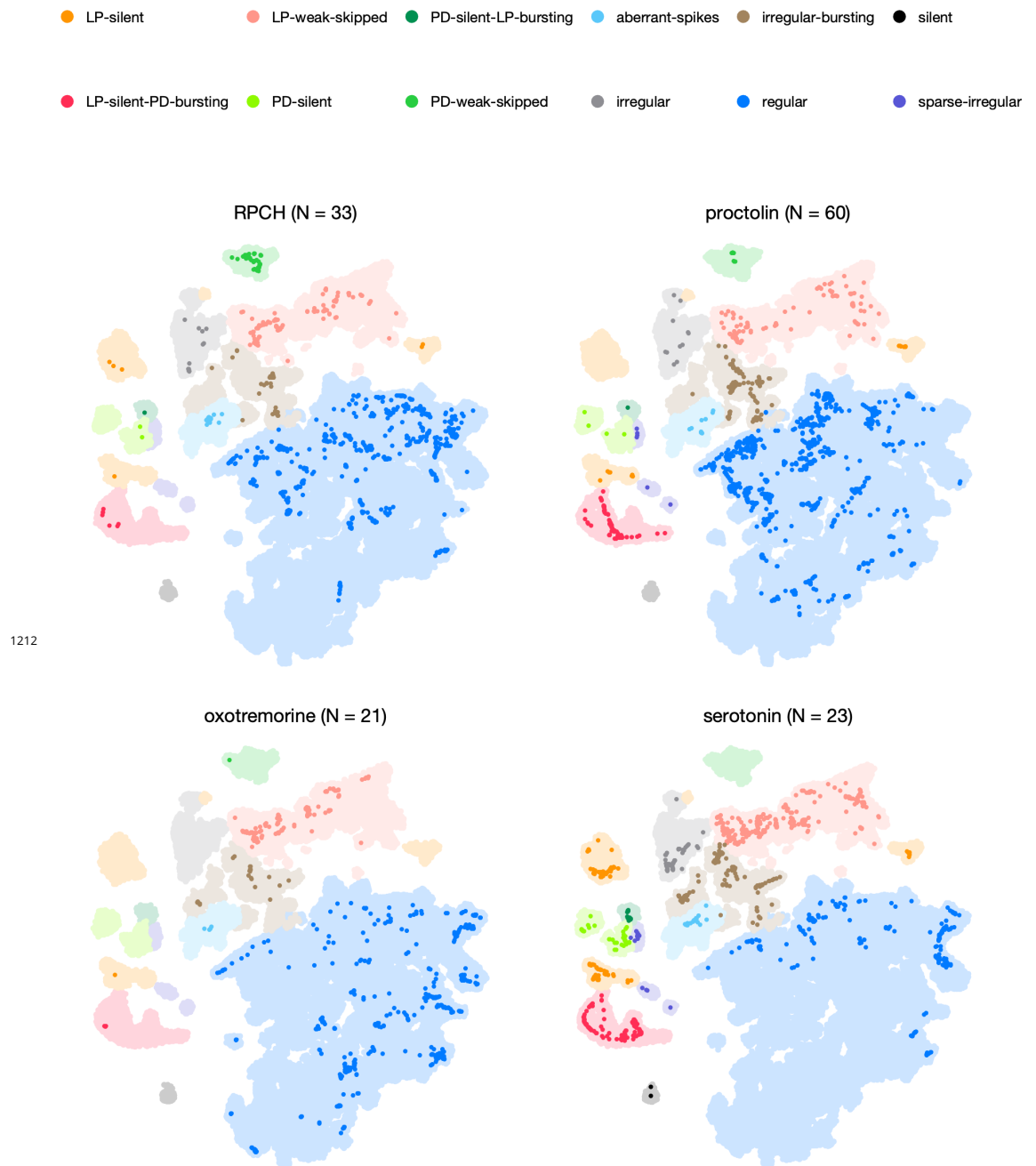


Figure 9-Figure supplement 2. Neuromodulators affect map occupancy. In each panel, all the data are shown in light shading. Bright colors indicate distribution of data during bath application of that neuromodulator. The number of animals in each panel is indicated in the title.